Constraints on Cumulus Parameterization from Simulations of Observed MJO Events

ANTHONY D. DEL GENIO

NASA Goddard Institute for Space Studies, New York, New York

JINGBO WU, AUDREY B. WOLF, AND YONGHUA CHEN

Department of Applied Physics and Applied Mathematics, Columbia University, New York, New York

MAO-SUNG YAO

Trinnovim LLC, Institute for Space Studies, New York, New York

DAEHYUN KIM

Department of Atmospheric Sciences, University of Washington, Seattle, Washington

(Manuscript received 6 December 2014, in final form 15 April 2015)

ABSTRACT

Two recent activities offer an opportunity to test general circulation model (GCM) convection and its interaction with large-scale dynamics for observed Madden–Julian oscillation (MJO) events. This study evaluates the sensitivity of the Goddard Institute for Space Studies (GISS) GCM to entrainment, rain evaporation, downdrafts, and cold pools. Single Column Model versions that restrict weakly entraining convection produce the most realistic dependence of convection depth on column water vapor (CWV) during the Atmospheric Radiation Measurement MJO Investigation Experiment at Gan Island. Differences among models are primarily at intermediate CWV where the transition from shallow to deeper convection occurs. GCM 20-day hindcasts during the Year of Tropical Convection that best capture the shallow–deep transition also produce strong MJOs, with significant predictability compared to Tropical Rainfall Measuring Mission data. The dry anomaly east of the disturbance on hindcast day 1 is a good predictor of MJO onset and evolution. Initial CWV there is near the shallow–deep transition point, implicating premature onset of deep convection as a predictor of a poor MJO simulation. Convection weakly moistens the dry region in good MJO simulations in the first week; weakening of large-scale subsidence over this time may also affect MJO onset. Longwave radiation anomalies are weakest in the worst model version, consistent with previous analyses of cloud/moisture greenhouse enhancement as the primary MJO energy source. The authors' results suggest that both cloud-/moisture-radiative interactions and convection–moisture sensitivity are required to produce a successful MJO simulation.

1. Introduction

The Madden–Julian oscillation (MJO; Madden and Julian 1971), a planetary-scale disturbance that propagates eastward at $\sim 5\,\mathrm{m\,s^{-1}}$, is the most important contributor to tropical subseasonal weather variability. It influences a wide variety of phenomena within and outside the tropics, including the Asian and Australian monsoons, El Niño, winter precipitation in the western United States, and tropical cyclones (see Zhang 2013 for a complete review).

Yet despite its practical significance, the MJO is of even more interest because its physical basis is not well understood (Zhang et al. 2013). Almost all other tropical large-scale wave modes observed via their effects on outgoing longwave radiation (OLR), and thus convection (Wheeler and Kiladis 1999), are predicted from shallow-water theory on an equatorial beta plane (Matsuno 1966). The MJO is not predicted by classical theory yet is prominent in the Wheeler and Kiladis (1999) analysis. This suggests that unlike other wave

Corresponding author address: Anthony D. Del Genio, NASA Goddard Institute for Space Studies, 2880 Broadway, New York, NY 10025.
E-mail: anthony.d.delgenio@nasa.gov

DOI: 10.1175/JCLI-D-14-00832.1

© 2015 American Meteorological Society

modes, which modulate and are modulated by convection but would still exist in a dry atmosphere, the MJO's existence is fundamentally tied to interactions among convection, moisture, clouds, and large-scale dynamics. Hence, it offers a useful test of whether cumulus parameterization physics is adequate to capture convective feedbacks on climate change (Del Genio 2012).

General circulation models (GCMs) generally fail this test (Lin et al. 2006; Hung et al. 2013; Jiang et al. 2015), with most simulating little or no MJO-like variability. For the few that do, it is not clear whether they do so with realistic physics. Many theories for the MJO exist, but in recent years evidence has accumulated for the interpretation of the MJO as a ''moisture mode''—that is, a dynamical mode based on prognostic humidity fluctuations in a weak temperature gradient environment and driven by sources of moist static energy (e.g., Neelin and Yu 1994; Raymond 2001; Majda and Stechmann 2009; Raymond and Fuchs 2009; Sobel and Maloney 2013).

In moisture mode theory, eastward MJO propagation depends on the buildup of moist static energy east of the disturbed, heavily precipitating phase of the oscillation and its collapse west of the disturbed phase (i.e., a source in quadrature with the MJO peak). It has been suggested that moistening by shallow and congestus convection is important to this buildup (e.g., Bladé and Hartmann 1993; Hu and Randall 1994; Kemball-Cook and Weare 2001; Benedict and Randall 2007). Such clouds are prevalent in the suppressed and developing stages of the MJO in observations (Lin and Johnson 1996; Morita et al. 2006; Chen and Del Genio 2009; Lau and Wu 2010; Tromeur and Rossow 2010; Riley et al. 2011; Del Genio et al. 2012a; Barnes and Houze 2013; Powell and Houze 2013; Zuluaga and Houze 2013; Xu and Rutledge 2014). Significant moistening by these clouds has been observed before MJO onset (e.g., Ruppert and Johnson 2015), though for individual events the buildup may be faster than suggested by composites over many events (Powell and Houze 2013). Shallow convection is not a net-column moist static energy source, but its bottom-heavy heating induces a circulation that can import moist static energy and may create negative gross moist stability, destabilizing the MJO (e.g., Raymond et al. 2009). Large-scale advective moistening in advance of the MJO peak may thus be ultimately responsible for MJO eastward propagation (Maloney 2009; Kiranmayi and Maloney 2011; Andersen and Kuang 2012; Sobel and Maloney 2013; Kim et al. 2014; Sobel et al. 2014).

Viewed from the moisture mode perspective, the failure of most GCMs to simulate the MJO can be traced to deficiencies in their representation of the interaction between convection and humidity. Most cumulus parameterizations are insufficiently sensitive to tropospheric humidity because of weak entrainment (Derbyshire et al. 2004), and, conversely, relatively little attention has been paid to the ability of cumulus parameterizations to moisten rather than dry the environment when convection is shallow (Klingaman et al. 2015a,b). Thus, a typical GCM prematurely transitions from shallow to deep convection during the suppressed phase, and the resulting elevated heating and divergent circulation export moist static energy, stabilizing rather than destabilizing the column (Raymond et al. 2009). Numerous climatological GCM studies have shown that cumulus parameterizations with stronger entrainment and/or convective rain evaporation can successfully reproduce many aspects of the MJO (e.g., Tokioka et al. 1988; Kim et al. 2009; Hannah and Maloney 2011; Kim et al. 2012; Chikira and Sugiyama 2013), albeit usually with a degraded mean climate (Kim et al. 2011b).

Even if gross moist stability is weakly positive, the MJO may be destabilized by a moist static energy source such as radiative (primarily longwave) heating of the column or surface turbulent (primarily latent heat) fluxes. Mechanism-denial experiments suggest that radiative heating anomalies due to enhanced high cloud during the MJO onset and disturbed phase are important (Andersen and Kuang 2012; Kim et al. 2011a), and observations support this (Lin and Mapes 2004; Stephens et al. 2004; Tromeur and Rossow 2010; Ma and Kuang 2011; Sobel et al. 2014). The role of surface turbulent fluxes is less clear. Latent heat flux anomalies peak during the westerly wind burst period after the MJO peak (Tromeur and Rossow 2010) but are still somewhat positively correlated with moist static energy (Sobel et al. 2014). Kim et al. (2015) find that GCMs with stronger longwave cloud-heating anomalies during phases of the MJO with weak positive rain anomalies have stronger MJOs than those with weaker longwave anomalies.

Until recently, MJOs in climate GCMs have usually been evaluated in climatological simulations for which only the statistics of many events can be compared to observations. Thus, predictability of specific observed MJO events cannot be assessed, nor is it straightforward to determine whether the biased mean state in most successful MJO simulations is a side effect or central to the emergence of the model MJO. In this paper we exploit two recent community activities that allow GCM MJOs to be evaluated on weather time scales. A Single Column Model (SCM) version of the National Aeronautics and Space Administration (NASA) Goddard Institute for Space Studies (GISS) GCM is used to simulate convection–humidity interactions during the Department of Energy Atmospheric Radiation

Measurement MJO Investigation Experiment (AMIE) at Gan Island in the Indian Ocean that took place in conjunction with the Dynamics of the MJO (DYNAMO) field experiment in 2011. We then use 20-day hindcasts of the full GCM initialized by analyses from the Year of Tropical Convection (YOTC) Vertical Structure and Diabatic Processes of the MJO project in conjunction with satellite data from the NASA Tropical Rainfall Measuring Mission (TRMM) to test the simulated spatial and temporal evolution of an observed MJO event in 2009. We focus in this study on how cumulus parameterization affects the MJO onset phase. Section 2 describes the data sources and model versions used in the analysis. SCM results for the AMIE period are described in section 3, and GCM YOTC hindcast results are presented in section 4. The implications of our results for understanding the MJO and for future cumulus parameterization development are discussed in section 5.

2. Data and models

a. AMIE-Gan/DYNAMO field campaign

We drive the SCM with the AMIE-Gan large-scale forcing and evaluation product derived by the ARM program for the period 0000 UTC 2 October 2011 to 2100 UTC 31 December 2011, covering two complete DYNAMO MJO events (Gottschalck et al. 2013; Johnson and Ciesielski 2013; Yoneyama et al. 2013). The forcing uses the constrained variational objective analysis (CVA) method (Zhang et al. 2001). CVA recognizes that any sounding- or analysis-based estimate of large-scale advective tendencies contains errors that affect a model that is driven by them. It therefore adjusts the advective tendencies and large-scale vertical velocities from a sounding array or an analysis product by the minimum amount required for the column mass, moisture, static energy, and momentum budgets to be consistent with observations of top-of-atmosphere radiative fluxes, surface radiative and turbulent fluxes and pressure, and precipitation.

CVA is typically applied to forcing estimates derived from a sounding array, but the lack of adequate surface flux data and the large distance (7°–8°) between sounding locations for the Gan area made this nonoptimal. This was particularly so because surface precipitation is the strongest constraint on the large-scale vertical velocity adjustment derived from CVA, and the coverage area of the DYNAMO rain radars was much less than the area within the sounding array. Thus, 0.25°-resolution European Centre for Medium-Range Weather Forecasts (ECMWF) operational analyses were used instead for the original forcing estimate and adjusted using either DYNAMO surface Shared Mobile Atmospheric Research and Teaching Radar (SMART-R) (DePasquale et al. 2014) or satellite (TRMM 3B42; Huffman et al. 2007) precipitation retrievals, producing two independent forcing products. The ECMWF-based forcing domain is taken to be the 300-km diameter range of the SMART-R radar, but the radar's view was partially obscured, so ARM also provides a third, adjusted SMART-R rain product. This product uses the TRMM data to account for rain rates in the area unviewed by SMART-R. The "adjusted SMART-R" product is defined as the actual SMART-R rain rate divided by the ratio of the TRMM rain rate within the SMART-R area to the TRMM rain rate over the entire forcing domain. All three products capture the basic variability of rain during the MJO but give very different rain rates, and thus vertical velocity forcing, on the 3-h time scale (Fig. 1). The forcing products also provide atmospheric state evaluation data that we use to estimate vertical thermodynamic structure and column water vapor (CWV). SCM temperature and humidity profiles are relaxed toward the observations with a short 3-h relaxation time to permit us to evaluate the response of SCM convection to something close to observed large-scale atmospheric conditions. Strong relaxation partially decouples the SCM response from the forcing large-scale vertical velocity. Thus SCM convection can deviate significantly from that observed and be diagnostic of cumulus parameterization deficiencies (Song et al. 2013), unlike when the constrained variational analysis is applied directly.

We also use data from the Ka-band (35 GHz) ARM Zenith Radar (KAZR) deployed at Gan during AMIE to estimate convective cloud top heights and their relationship to CWV. A background mean reflectivity profile is calculated from a clear-sky time interval, and clouds at other times are identified at altitudes for which the reflectivity exceeds the background. We identify 15-min intervals during which cloud base altitude <2 km at any time during the period. The first reflectivity-based cloud top above that base is identified as the convective cloud top, under the assumption that continuous columns of cloud rooted in the boundary layer in this region are convective rather than stratocumulus or nimbostratus clouds. If multiple cloud tops exist in a 15-min time interval the highest one is used. Time periods during which the Doppler velocity below the 0°C level (~4.1 km) is $<-1\ \mathrm{m\,s^{-1}}$ are assumed to be precipitation falling from elevated stratiform rain clouds rather than convective clouds and are excluded from our analysis.

Figure 2 shows an example for a day (28 November 2011) with a mix of shallow, congestus, deep convective, stratiform rain, and nonprecipitating anvil clouds. The

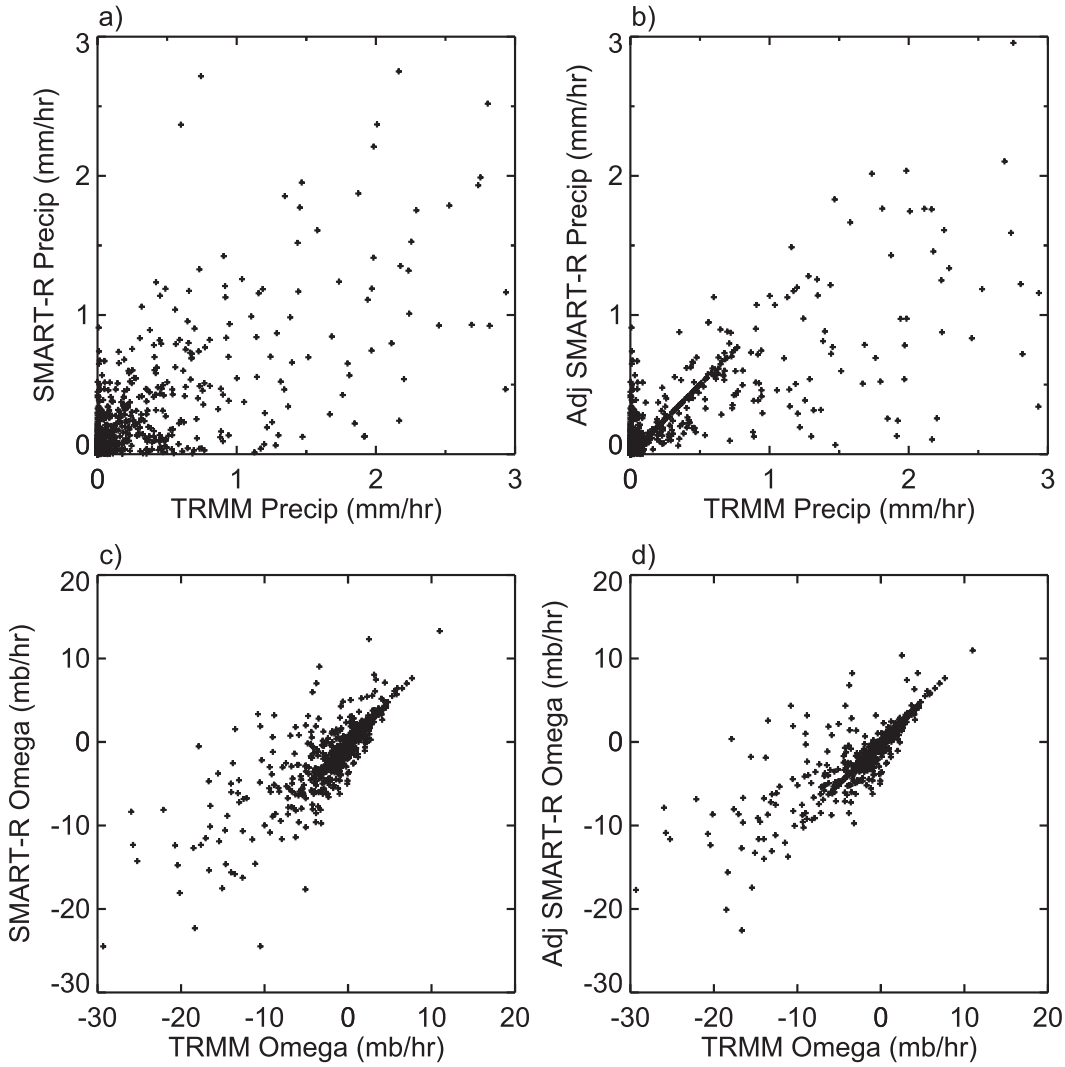

FIG. 1. (top) Scatterplots of (left) 3-h SMART-R and (right) adjusted SMART-R precipitation rates vs TRMM 3B42 precipitation rates over the AMIE-Gan period. (bottom) As in the top panels but for 700-hPa pressure vertical velocity derived using each rain product as the constraint to adjust the ECMWF vertical velocity.

detection procedure has some limitations. Some of the shallowest cloud detections may be instantaneous noise that rises above the background (e.g., 1500–1700 UTC), but many are likely to be real shallow clouds. On the other hand, since equatorial low clouds form preferentially on small islands (McFarlane et al. 2005), the KAZR sample of such clouds may be biased high relative to the mostly oceanic domain being simulated by the SCM. Brief periods of high low-level reflectivity and midlevel cloud top (0200, 0600–0700 UTC) that may be weak congestus are excluded by the negative Doppler velocity criterion. Occasionally a nonprecipitating anvil overlapping a lower congestus cloud (1000–1100 UTC) is falsely identified as deep convective. Our interest, however, is in the statistics of the transition from shallow to deep convection over several months, and our procedure captures this transition satisfactorily compared to previously published results (section 3).

b. *Hindcast initialization and MJO index*

For the 20-day GCM hindcasts, we follow the protocol for the YOTC Vertical Structure and Diabatic Processes of the MJO intercomparison (Petch et al. 2011; Klingaman et al. 2015a). The ECMWF YOTC analysis is used to initialize the GCM daily for successive 20-day hindcasts during YOTC Event E. The GCM is forced by observed sea surface temperature (SST). Because we are interested in processes that affect MJO initiation and propagation, we focus on 6 consecutive hindcasts (29 October 2009–3 November 2009) for which the

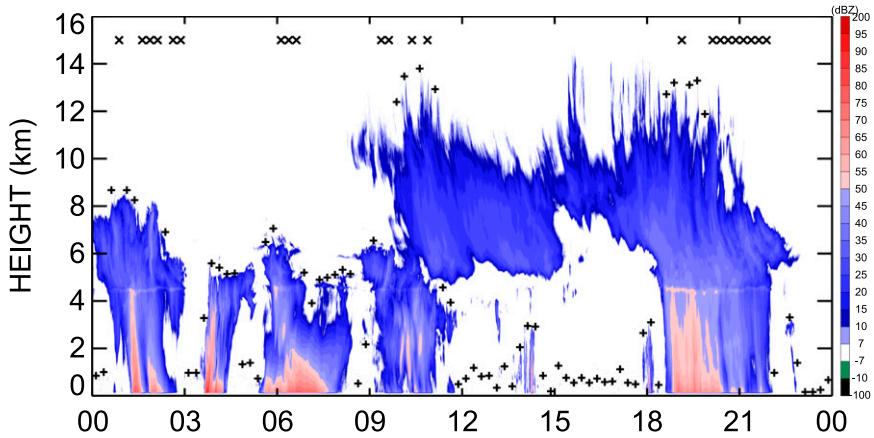

FIG. 2. Gan KAZR reflectivity profiles vs time (UTC) on 28 Nov 2011 (shaded). The + symbols indicate detections of convective cloud tops in 15-min time intervals, while the *x* symbols designate clouds that are defined as not being convective because of their significant downward Doppler velocity.

GCM is initialized during MJO Phase 1 as defined by the Wheeler and Hendon (2004) index. For the analysis presented here, we create composite 20-day Hovmöller diagrams by averaging fields for the 6 individual hindcasts and then calculate anomalies by subtracting values averaged over all hindcasts and all 20 days of each hindcast at each longitude.

c. *TRMM satellite data during YOTC*

We use three TRMM rain rate products to assess the robustness of the hindcast MJO signal. The TRMM and Other Satellites (3B42) Version 7 dataset combines TRMM Microwave Imager (TMI) and Visible and Infrared Scanner data with information from 6 operational satellites to produce a global gridded dataset at daily resolution (Huffman et al. 2007). For TMI we use the Version 4 rain rate and CWV products of Wentz (1997). For the TRMM Precipitation Radar (PR), we use the Version 7 2A25 rain-rate and storm-height (radar echo-top altitude) products (Iguchi et al. 2000). For the TMI and PR data, which do not cover all longitudes in a single day, we calculate daily running means of 3-day averages.

Figure 3 shows Hovmöller diagrams of 3B42, TMI, and PR equatorial (5°N–10°S) rain rate anomalies and PR storm-height anomalies for longitudes 65°–170°E during YOTC MJO Event E beginning in late October 2009. The MJO is visible in all TRMM products as a slowly ($\sim 5\,\mathrm{m\,s^{-1}}$) eastward-propagating region of enhanced convection starting in the west Indian Ocean. The PR MJO signal is the noisiest, because of sparse sampling due to the narrower PR cross-track swath and the greater PR sensitivity to details of the vertical structure. Nonetheless, a clear storm-height signal is present, with fluctuations of ~3–4 km from the disturbed to the suppressed phase of the MJO. This event therefore appears to present a good test for a cumulus parameterization's ability to capture the transition from shallow to deep convection.

d. *Other validation datasets*

To assess the realism of GCM moist static energy sources, we use the International Satellite Cloud Climatology Project (ISCCP) radiative flux product (Zhang et al. 2004) to calculate MJO OLR anomalies for the 2009 YOTC event, and the objectively analyzed air–sea fluxes (OAFlux) product (Yu et al. 2008) for surface latent heat fluxes for this event.

e. *Cumulus parameterization tests*

We use the GISS Model E2 GCM (Schmidt et al. 2014) at 2°×2.5°×40L resolution as the baseline for all simulations. A full description of the Model E2 cumulus parameterization can be found in Kim et al. (2013); we summarize it below.

The Model E2 cumulus parameterization uses a mass flux closure with the mass flux determined by the mass required to establish neutral buoyancy at cloud base over a specified adjustment time (currently 1 h). The total mass flux is divided into two components ("plumes") that entrain at different rates ε (Del Genio et al. 2007). Entrainment follows Gregory (2001), with $\varepsilon = CB/w^2$, where B is parcel buoyancy including condensate loading, w is the diagnosed updraft speed following Gregory (2001), and C is a constant representing the fraction of the buoyant turbulent kinetic energy production that is available for entrainment. Convection is triggered when a parcel, lifted one model layer, becomes buoyant according to a virtual moist static energy

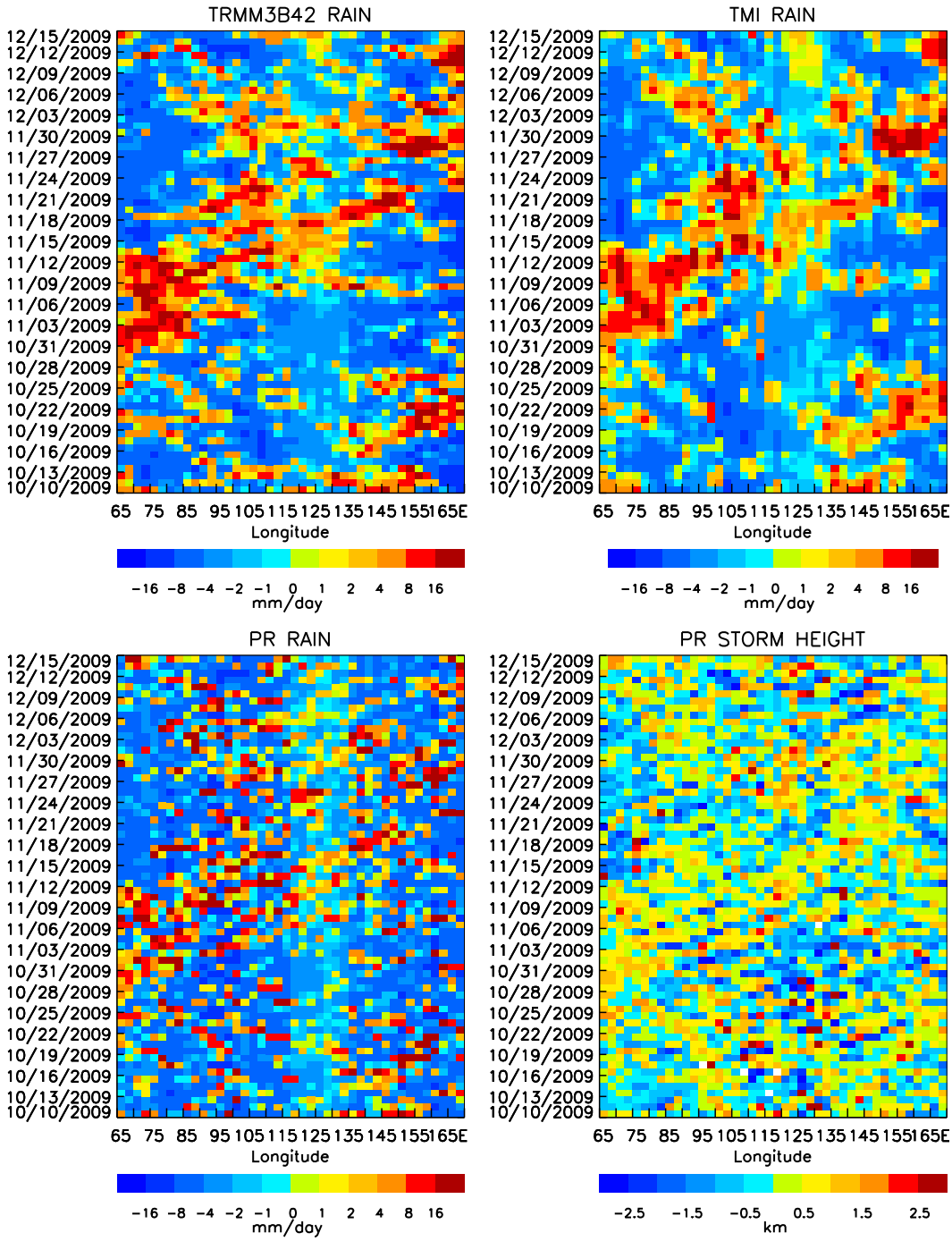

FIG. 3. Hovmöller diagrams over the YOTC boreal autumn period of (top left) TRMM 3B42, (top right) TMI, and (bottom left) PR precipitation rate anomalies and (bottom right) TRMM PR storm-height anomalies.

test. The initial parcel vertical velocity is derived from the boundary layer turbulent kinetic energy, and the plume rises until the updraft speed decreases to zero. Mass is detrained at all levels above the level of neutral buoyancy. A downdraft forms at any level when an equal mixture of cloud and environment is negatively buoyant; it entrains at a rate of $0.2\,\mathrm{km}^{-1}$ as it descends. A prescribed fraction of the convective precipitation is incorporated into the downdraft and available for evaporation. Downdraft air that reaches the boundary

layer mixes with the environment there. Updraft convective condensate is partitioned into fractions that precipitate, detrain, and are carried upward by assuming a Marshall–Palmer particle size distribution and empirical size–fall speed relationships and calculating the fraction of the size distribution whose fall speed exceeds, is comparable to, or is less than the diagnosed updraft speed (Del Genio et al. 2005). Detrained condensate is treated by the stratiform cloud microphysics (an updated version of Del Genio et al. 1996). Momentum is transported by convection following Gregory et al. (1997).

For this paper, we consider 4 variants of the baseline parameterization:

1) AR5: This is the basic parameterization described in Schmidt et al. (2014) used for GISS phase 5 of the Coupled Model Intercomparison Project simulations and for the Intergovernmental Panel on Climate Change Fifth Assessment Report. For this paper the key features of this model version are that (i) the entrainment constant has the values $C_1 = 0.3$ and $C_2 = 0.6$ for the less-entraining and more-entraining plumes, respectively; (ii) 100% of the convective precipitation is made available to the downdraft for evaporation; (iii) downdraft buoyancy is assessed only on the basis of temperature; and (iv) the fraction of the total mass flux in plume 1 is determined by the grid-scale low-level convergence. This version is known to produce very little MJO variability when used in a climatological GCM simulation (Kim et al. 2012).
2) Stronger entrainment: In this version, C_1 is increased to 0.4, 50% of the convective precipitation is made available to evaporate directly into the grid-scale environment rather than the downdraft, downdraft buoyancy is based on virtual temperature including condensate loading, and an artificial limit on the cumulus mass flux in any layer is removed. This model version produces significant MJO-like variability in climatological simulations; the increase in entrainment alone is sufficient to produce an MJO (Kim et al. 2012).
3) Cold pool I: Although the stronger-entrainment GCM simulates an MJO, A-Train satellite data suggest that plume 1 (which captures the deepest convection) occurs too often at intermediate CWV (Del Genio et al. 2012a). Cloud-resolving models suggest that the onset of weakly entraining deep convection often begins at the gust fronts of downdraft cold pools formed from prior events (Tompkins 2001; Khairoutdinov and Randall 2006; Del Genio and Wu 2010; Böing et al. 2012; Schlemmer and Hohenegger 2014). Mapes (2000) notes that the usual GCM approach of mixing cold downdraft air with ambient boundary layer air artificially terminates convection rather than stimulating it. The effects of cold pools can be parameterized either by modifying existing convection parameters (Piriou et al. 2007; Mapes and Neale 2011; Hohenegger and Bretherton 2011) or by creating explicit subgrid cold pools that evolve in time (Qian et al. 1998; Grandpeix and Lafore 2010; Park 2014; Schlemmer and Hohenegger 2014).

   We have developed a simple experimental cold pool parameterization to regulate the occurrence of weakly entraining convection in a more physically based fashion than the stronger-entrainment model. Plume 1 does not form until the time step after downdraft air enters the boundary layer with a virtual potential temperature θ_v colder than the ambient air and a mass of at least 5% the mass of the boundary layer. At this time a cold pool is defined; details are given in the appendix. Cold pool depth evolution is determined by downdraft mass added at future time steps and the horizontal spread rate of the cold pool. Once downdrafts terminate, plume 1 continues to exist if ambient air (which remains distinct from the cold pool air) lifted to the altitude of the cold pool top becomes buoyant. The cold pool terminates when its thermodynamic properties become similar to those of the ambient boundary layer.
4) Cold pool II: The parameterization described above produces plume 1 very infrequently, as discussed in section 4. We therefore introduced other changes designed to increase downdrafts and cold pools to understand how this affects MJO evolution. Downdraft mass flux was increased in several ways: by changing the initial 50–50 mixture of cloud and environment air to the proportions that produce maximum negative buoyancy, by increasing the amount of precipitation permitted to evaporate in the downdraft in each layer from that produced locally in that layer to that accumulated from all higher layers, and by increasing the entrainment rate in the downdraft from 0.2 to 0.5 km^{-1}. This experiment also uses a slightly modified boundary layer turbulence scheme that produces more realistic boundary layer depths (Yao and Cheng 2012); the initial cold pool depth is assumed to be the depth of the boundary layer.

Parameterization changes typically drive GCMs out of global radiation balance (e.g., Mauritsen et al. 2012), which leads to global precipitation biases. We adjust free

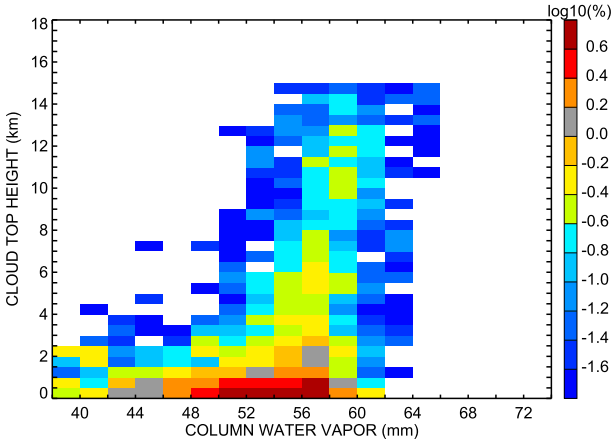

FIG. 4. Histogram of Gan KAZR convective cloud-top height occurrence frequency as a function of column water vapor from the AMIE forcing product for the period 0000 UTC 8 Oct 2011 to 2100 UTC 31 Dec 2011.

parameters that determine the threshold relative humidity at which stratiform clouds form to restore each model version to radiation balance. This reduces some of the mean-state degradation noted in previous GCM studies of the effect of parameterization changes on the MJO, a necessary step before such a model can be used operationally. For example, the parameterization changes in the stronger-entrainment simulation increase high and low cloud cover relative to AR5 and create a global (primarily shortwave) imbalance of $-7\,\mathrm{W\,m^{-2}}$. The adjustment in threshold relative humidity we apply to restore balance appears to slightly weaken the simulated MJO, but the effect is minor and is clearly not the reason this simulation develops an MJO while AR5 does not.

3. SCM simulations

a. Sensitivity of convection depth to humidity

Figure 4 shows the occurrence of KAZR convective cloud top height (CTH) as a function of CWV from the TRMM-based forcing data for the AMIE-Gan period. Convection is almost always shallow (CTH $<$ 4 km) for CWV $<$ 50 mm. For 50 $<$ CWV $<$ 54 mm, occasional congestus and deep convection are observed, and at higher CWV all three types of convection are common. This behavior is consistent with a spaceborne radar–lidar climatology of CTH for 5 years of MJO events over the warm pool region (Del Genio et al. 2012a) and with surface cloud radar estimates at Nauru Island (Jensen and Del Genio 2006). The primary difference is that the KAZR heights rarely exceed 15 km, whereas the satellite data show peak CTH occurrence for deep clouds at 15–16 km and some tops as high as 18 km. Some of this difference may be real, since the deepest convection occurs more often over the west Pacific than the Indian Ocean because of geographic differences in thermodynamic structure (Kelley et al. 2010). There may also be a detection issue, since spaceborne lidar is very sensitive to CTH whereas the KAZR attenuates near the tops of heavily precipitating convective cells (DePasquale et al. 2014). Some of the detected cloud tops may be instantaneous snapshots of convective clouds in the process of rising to deeper levels; however, a similar analysis of spaceborne radar–lidar data for the wettest regions of the tropical warm pool with frequent deep convection suggests that the contribution from so-called transient convective cloud top detections cannot be very large (Del Genio et al. 2012a).

Figure 5 shows corresponding frequency histograms for the four SCM versions driven by the TRMM-based forcing. AR5 (Fig. 5, top left) produces some deep convection for CWV $<$ 50 mm, where KAZR sees little, and deep convection dominates in the SCM for 50 $<$ CWV $<$ 54 mm, where deep convection occurs occasionally in the KAZR data but much less often than shallow events. This is consistent with AR5's weaker entrainment and inadequate convection sensitivity to tropospheric moisture, and it is plausibly related to the failure of the parent GCM to simulate the MJO. The stronger-entrainment version of the SCM (Fig. 5, top right) convects somewhat less deeply for 40 $<$ CWV $<$ 50 mm, with fewer events reaching 9–12-km altitude, but otherwise behaves similarly to the AR5 simulation. The fact that the parent GCM of this model version produces MJO variability while the AR5 version does not (Kim et al. 2012) highlights the intermediate CWV transition regime as a key to the existence of the MJO.

The cold pool I SCM (Fig. 5, bottom left) is very successful at reproducing the features of the KAZR-observed CTH–CWV distribution, with almost no deep convection for CWV $<$ 50 mm, a gradual deepening from 50 to 54 mm, and very little shallow convection for CWV $>$ 62 mm. This model most severely restricts the occurrence of plume 1, supporting the impression from numerous studies that entrainment is usually much stronger than GCMs have traditionally assumed (Derbyshire et al. 2004; Khairoutdinov and Randall 2006; Del Genio and Wu 2010; Sherwood et al. 2013). The cold pool II SCM (Fig. 5, bottom right) is slightly less successful, producing more deep convection in the 48 $<$ CWV $<$ 54 mm range than is observed, but it performs better than the other two model versions. Note also that the highest convective cloud tops in all four SCMs are 1–2 km lower than those detected by KAZR. The AR5 model is most realistic in this respect,

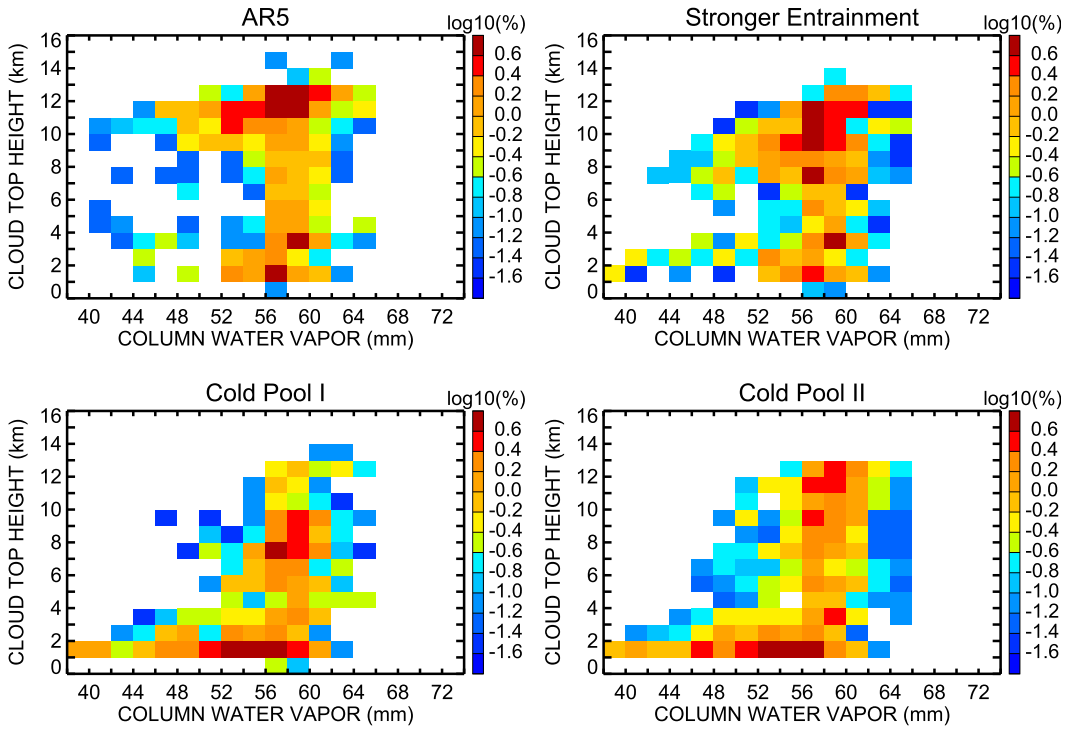

FIG. 5. As in Fig. 4, but for the SCM for 0000 UTC 2 Oct 2011 to 2100 31 Dec 2011. (top left) AR5; (top right) stronger entrainment; (bottom left) cold pool I; (bottom right) cold pool II.

reflecting the emphasis through most of GCM cumulus parameterization history on producing convection that reaches the tropopause.

TRMM 3B42 has heavier rain rates than SMART-R and thus stronger upward vertical velocities (Fig. 1) and moistening tendencies when used in the constrained variational analysis (Xie et al. 2004). As a result, the CTH–CWV histogram for runs with the SMART-R forcing (not shown) are generally shifted toward lower CWV but otherwise fairly similar in shape. This behavior is reduced when the adjusted SMART-R forcing is used instead, but nonnegligible differences of this type still exist. The conclusion remains, however, that the cold pool I SCM performs best against this metric of convection sensitivity to moisture.

Figure 6 shows entrainment rate profile histograms for the AR5 SCM (Fig. 6a) and differences between different model versions (Figs. 6b–d). AR5 (Fig. 6a) has strong entrainment in the lower troposphere, but mostly $\varepsilon < 10\%\ \mathrm{km}^{-1}$ above that. The AR5 model arbitrarily limits the plume mass at any level to the mass of the cloud-base layer. When this occurs (in situations with vigorous cloud-base mass fluxes), entrainment is set to zero to prevent further mass increase. Incidences of this behavior can be seen in Fig. 6a. By itself this does not prevent the GCM from producing an MJO, but it contributes to some of the model behavior seen later in the paper. The stronger-entrainment model eliminates this limit (hence the decrease in ε occurrences at the far left of Fig. 6b) and generally shifts the entrainment rate profile to higher values at most altitudes relative to AR5. Cold pool I more dramatically increases ε at all levels to values $> 10\%\ \mathrm{km}^{-1}$ relative to the stronger-entrainment model (Fig. 6c), while cold pool II partly offsets the entrainment increases of cold pool I (Fig. 6d).

b. *Effect of convection and clouds on thermodynamic structure*

Since we relax SCM temperature and humidity toward the observations on a short time scale, the relaxation term is diagnostic of errors in the parameterized physics. In the boundary layer, subgrid turbulence dominates the error. Thus the sum of the relaxation term and the turbulence tendency provides an estimate of the errors due to moist convection, stratiform clouds (including anvils), and to a lesser extent radiation (for temperature only).

Figure 7 shows this sum for water vapor as a function of CWV. It can be interpreted as the rate at which the profiles must be adjusted to compensate for convection and cloud errors. In AR5 (Fig. 7a), the low/middle and middle/upper free troposphere are moistened by the

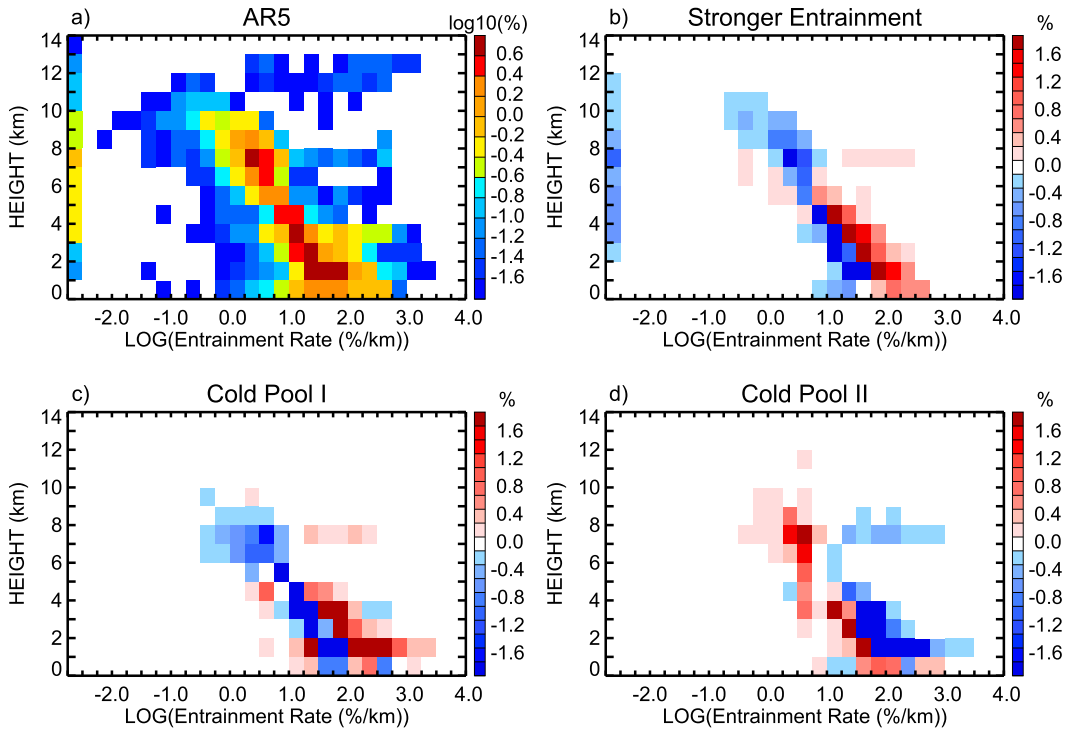

FIG. 6. (a) SCM entrainment rate vs altitude histogram for AR5; (b) stronger entrainment minus AR5; (c) cold pool I minus stronger entrainment; (d) cold pool II minus cold pool I. Points at the far left represent instances of zero entrainment. In (b)–(d), red shades indicate more occurrences of specific entrainment rate values at specific altitudes relative to the previous experiment, and blue shades indicate fewer occurrences. Thus, blue to the left and red to the right indicates that the parameterization change in question has shifted the distribution of entrainment rates to higher values.

relaxation for CWV $<$ 54 mm and $>$ 58 mm, respectively. This is evidence that convection penetrates too deeply and thus overly dries the troposphere. The stronger-entrainment model (Fig. 7b) reduces these errors, especially for high CWV. In the boundary layer, shallow convection penetrates ~25 mb too high, creating a dipole error near 900 hPa in both models. This can also be seen by comparing the low-level cloud distribution in the top panels of Fig. 5 to that in Fig. 4. Below 700 hPa, relaxation dries at high CWV, suggesting excess convective rain evaporation. For cold pool I (Fig. 7c), the free troposphere errors are even smaller, indicating that suppression of weakly entraining convection is a step toward realism, while cold pool II (Fig. 7d) degrades the situation somewhat. Both cold pool models reduce boundary layer moisture errors at intermediate CWV, while cold pool II also reduces them at high CWV. Given that SCM PBL clouds have higher tops than those detected by the KAZR, the behavior in Figs. 7c,d may indicate that shallow convection is partly compensating for errors in PBL vertical transport.

The corresponding temperature adjustments (not shown) are generally consistent with the moisture adjustments (i.e., relaxation cools the free troposphere, especially for high CWV), since excessive convective drying implies excessive heating as well. Likewise, relaxation heats the lower part of the boundary layer at high CWV, another sign of rain evaporation errors. One error that appears in temperature but not humidity is a small free troposphere warming relaxation tendency for 54 $<$ CWV $<$ 60 mm; this may be due to underestimated cloud-radiative heating.

4. GCM hindcasts

a. Precipitation and water vapor anomalies

The full GCM with the same four cumulus parameterization versions was run for 20-day hindcasts beginning on 6 consecutive days during Wheeler–Hendon phase 1 of the 2009 YOTC MJO Event E. Figure 8 shows composite Hovmöller diagrams of precipitation rate anomalies for the equatorial warm pool for the TMI data for each 20-day period and for the four GCM versions. In TMI (Fig. 8a), Event E is seen to begin as a stationary region of convection in the west Indian Ocean

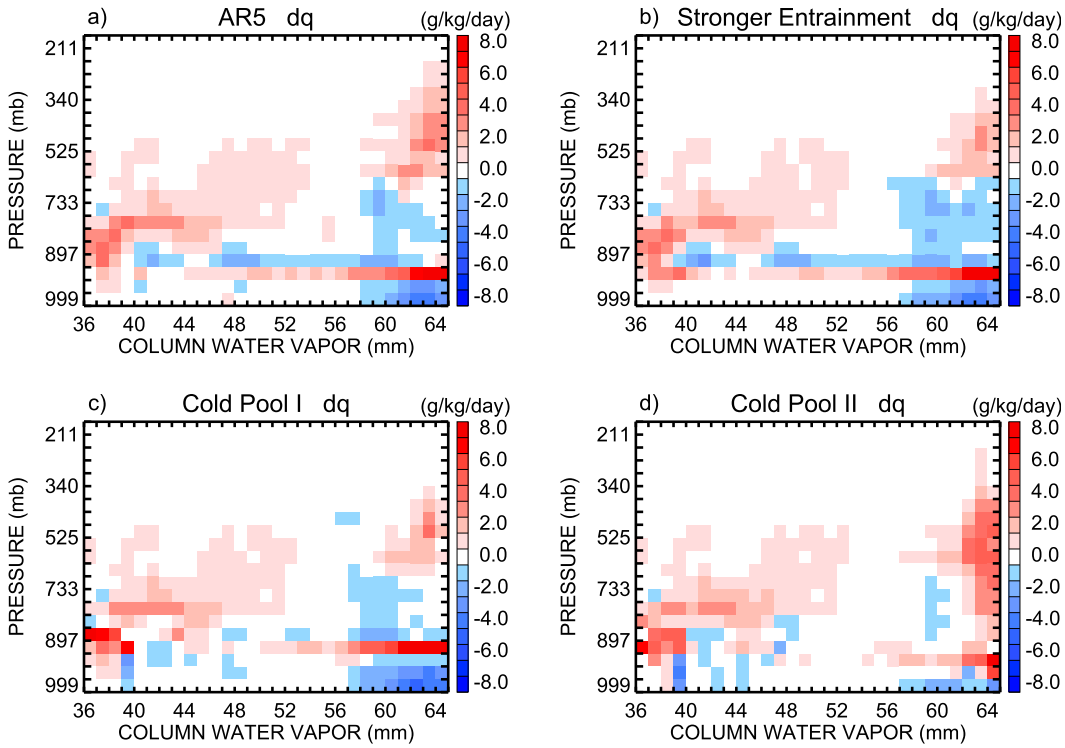

FIG. 7. Composite vertical profiles of the sum of the specific humidity relaxation rate and the tendency from the subgrid turbulence parameterization for the (a) AR5, (b) stronger entrainment, (c) cold pool I, and (d) cold pool II SCM versions. The numbers and tickmarks on the *y* axis represent the pressure levels of the SCM layers.

(65°–85°E) for approximately the first week, with suppressed conditions to the east, and then begins slowly propagating eastward in the second week. It appears to interact with a westward-propagating wave as it reaches the Maritime Continent at the end of the second week and eventually emerges in the west Pacific, at a somewhat faster propagation speed.

The AR5 GCM (Fig. 8b) shows only the faintest MJO—a broad, disorganized region of weak rain anomalies that moves eastward over the hindcast. What organization exists is more evident in simultaneous westward-propagating waves. In the observations, enhanced convection takes a day or two to break out in the west Indian Ocean, but the AR5 model responds to the hindcast initial conditions by immediately convecting over much of the Indian Ocean.

The stronger-entrainment GCM (Fig. 8c) is more successful. It correctly simulates the initial concentration of convection in the west Indian Ocean and the delay in the start of propagation for a week, and it produces reasonably suppressed conditions in the central-east Indian Ocean in the first week. The eventual propagation speed is slightly faster than observed, and by the third week precipitation predictability has decreased. But even by day 20 the hindcast shows some realism, though with weaker anomalies than observed. Cold pool I (Fig. 8d) is similar to the stronger-entrainment model but better in several ways, including stronger, more realistic rain anomalies in the final hindcast week and slightly slower propagation. Cold pool II (Fig. 8e) degrades the MJO somewhat by comparison, producing slightly faster propagation, weaker rain anomalies in the final hindcast week, and less suppressed conditions in the first week in the central-east Indian Ocean.

Table 1 provides some insights into the behavior of the different models. Recall that the cumulus parameterization consists of two plumes that share the mass flux, and that first and foremost the different models are characterized by how strongly the less-entraining plume (plume 1) entrains and by how often it occurs. In AR5, convection is almost equally divided between the two plumes. (Plume 1 is assumed not to exist only when low-level divergence is present, but this is infrequent in the convectively unstable, humid conditions in which a rising parcel can reach its level of free convection.) That does not change for the stronger-entrainment model, but the entrainment rate of plume 1 does. As in previous studies, the greater sensitivity of convection to tropospheric moisture limits convection depth and lowers the

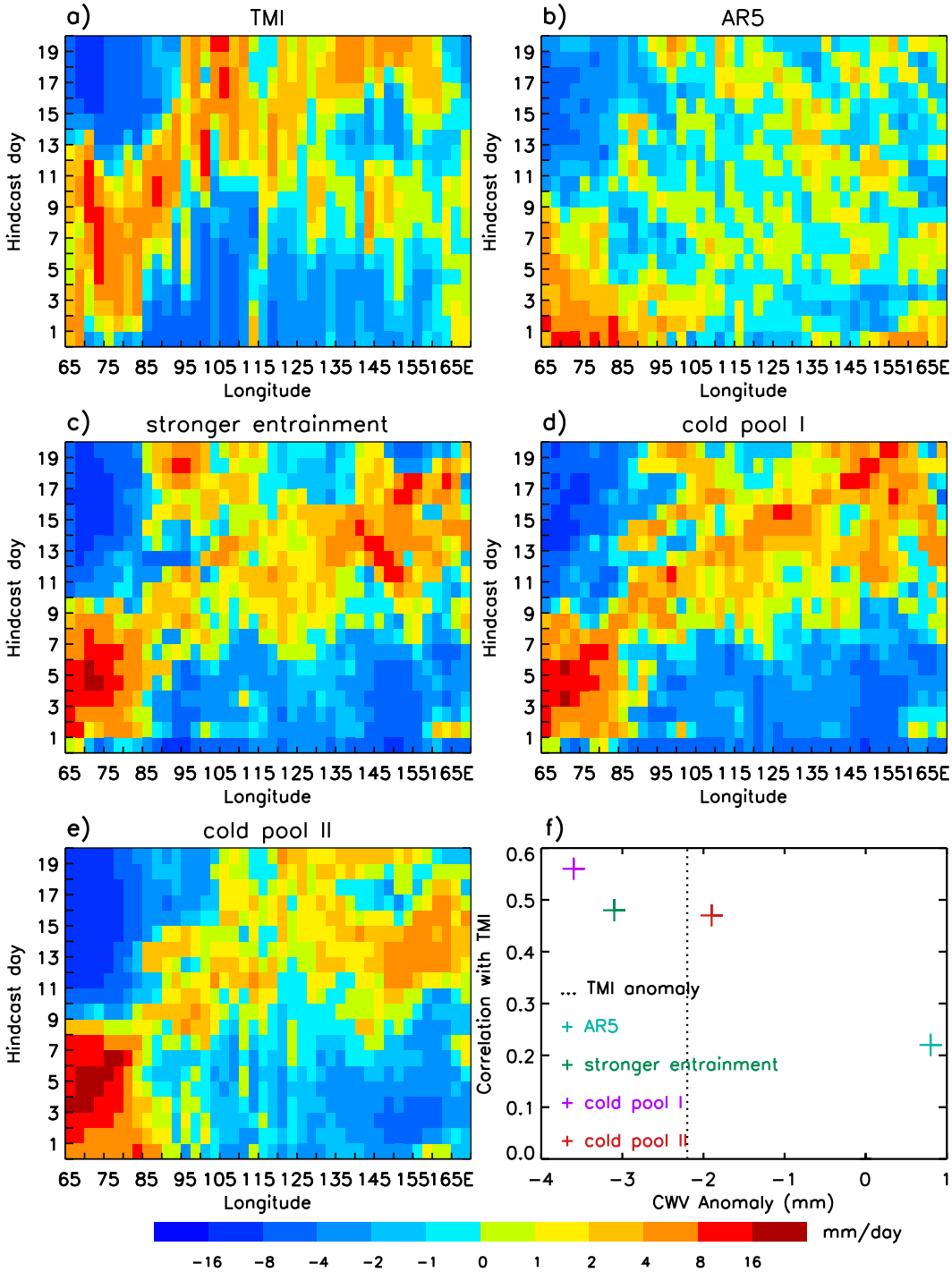

FIG. 8. Composite Hovmöller diagrams of precipitation rate anomalies starting on all 6 days during which the 2009 MJO Event E was in Wheeler–Hendon phase 1. (a) TMI data. (b) AR5 GCM hindcasts. (c) stronger-entrainment GCM hindcasts. (d) cold pool I GCM hindcasts. (e) cold pool II GCM hindcasts. (f) Pattern correlation of TMI rain anomalies with each model version vs day 1 CWV anomaly in the 85°–110°E region; the dotted line indicates the observed TMI CWV anomaly.

TABLE 1. Convection statistics for GCM hindcasts using the four different cumulus parameterization versions.

Model version	% of convective events in plume 1	Convection occurrence relative to AR5
AR5	48.5	1.00
Stronger entrainment	49.0	1.23
Cold pool I	7.6	1.28
Cold pool II	21.2	1.32

peak of convective heating during the drier stages of the MJO cycle, reducing the premature outbreak of deep convection ahead of the MJO peak. Increased rain evaporation makes the convection–humidity relationship two way, further strengthening the MJO, but the entrainment increase alone is sufficient to produce an MJO in this model (Kim et al. 2012). Note also in Table 1 that convection overall occurs 23% more frequently in this model than in AR5. This occurs because AR5 prematurely stabilizes the lapse rate and terminates convection too soon (Kim et al. 2012).

Cold pool I, on the other hand, drastically reduces the occurrence of plume 1, limiting it to times at which downdrafts and/or cold pools exist and are strong enough to trigger less-entraining convection. This is consistent with its more realistic dependence of convection depth on humidity in the AMIE-Gan SCM simulations (Fig. 5c). On the other hand, when plume 1 does exist, convection persists longer, since a secondary source of lifting is present and it draws from boundary layer air that has not been diluted by low moist static energy downdraft air. This produces a greater differentiation between suppressed and disturbed conditions but an overall increase in convection frequency (Table 1). The reason is that the convection now has memory of previous events due to prior downdraft and cold pool formation, departing further from quasi-equilibrium behavior (Davies et al. 2009). Cold pool II qualitatively does the same thing, but because it is designed to produce stronger downdrafts and deeper cold pools, plume 1 in this model occurs more often than in cold pool I—apparently too often, given the less suppressed conditions in the central-east Indian Ocean in the first hindcast week (Fig. 8e).

Figure 8 suggests that the behavior in the MJO buildup phase east of the disturbed region early in the hindcast is a harbinger of things to come. We calculated the pattern correlation between the TMI Hovmöller diagram (Fig. 8a) and that for each model version (Figs. 8b–e) as one simple measure of predictability. In Fig. 8f we plot the correlation versus the CWV anomaly on day 1 for 85°–110°E longitude, where TMI indicates negative rain anomalies, but the model rain responses differ significantly from each other. For reference, the TMI–PR pattern correlation is 0.70. The strength of the CWV anomaly on day 1 is seen to be a good predictor of the success of the simulation of subsequent MJO evolution, with cold pool I the best performer. This is consistent with Kim et al.'s (2014) conclusion that strong eastward MJO propagation is facilitated by anomalously dry conditions to the east. The stronger-entrainment GCM correlates with the data as well as or marginally better than cold pool I over the first 10 hindcast days (0.63 versus 0.61), but cold pool I outperforms the stronger-entrainment model over the final 10 days (0.52 versus 0.35). Note though that cold pool I produces the best MJO rain hindcast relative to the TRMM data at the expense of a larger dry anomaly in the central-east Indian Ocean than observed. Note also that the anomaly, not the mean state, diagnoses future evolution—AR5 is actually drier in total CWV (47.4 mm) in the 85°–110°E region than the other model versions (e.g., CWV = 49.6 mm for cold pool I). This is consistent with the idea that the MJO in this GCM is behaving like a moisture mode: maintenance of a dry anomaly east of the disturbed area is integral to the eastward propagation of the convective envelope that lies to the west of the dry anomaly.

To understand why the 85°–110°E initial behavior is key to MJO development in the hindcasts, Fig. 9 shows a Hovmöller diagram of TMI total CWV during Event E. During the first week of Event E (29 October 2009–3 November 2009) CWV ~ 50–56 mm in most of the 85°–110°E region, similar to the range over which the AMIE-Gan KAZR data (Fig. 4) indicate a rapid transition from shallow to congestus to deep convection. The climatology of TRMM PR storm height versus TMI CWV shows similar behavior (Fig. 10). Note that PR storm heights are mostly lower than KAZR cloud-top heights because the lower-frequency rain radar is sensitive only to large precipitating particles and not to the smaller cloud particles closer to cloud top (e.g., Jensen and Del Genio 2003). Thus the 85°–110°E region east of the disturbed area is really an intermediate CWV threshold area in which parameterized convection depth is highly sensitive to the interaction between the convective updraft and the tropospheric humidity.

b. *Convective heating/drying and dynamical evolution*

How do convection and the dynamics interact to produce MJO onset? Figure 11 shows vertical–longitudinal cross sections of moist convective heating and drying for day 1 of the AR5 and cold pool I simulations. AR5 produces top-heavy heating and strong drying in the west Indian Ocean disturbed region and

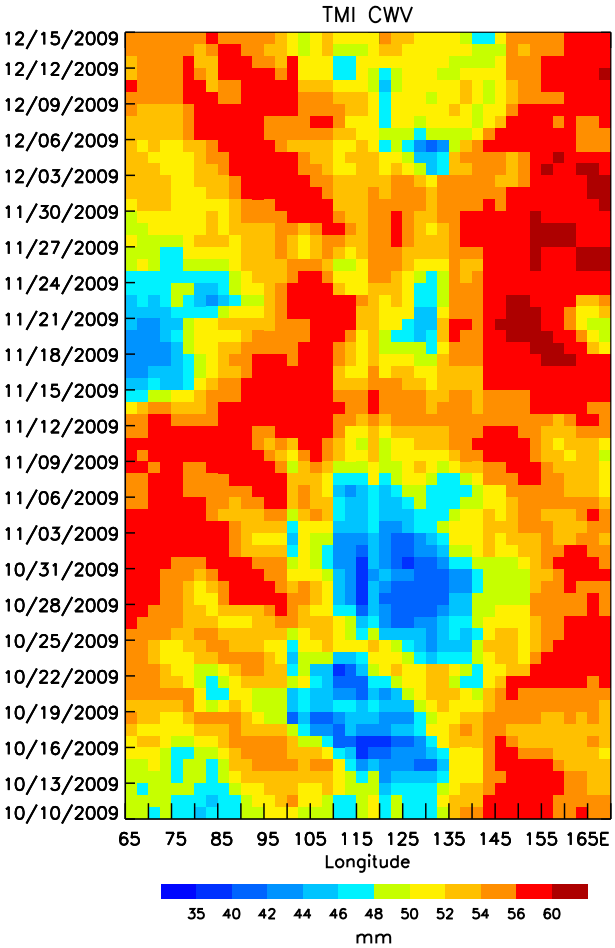

FIG. 9. Hovmöller diagram of TMI CWV evolution for YOTC MJO Event E over the equatorial warm pool region.

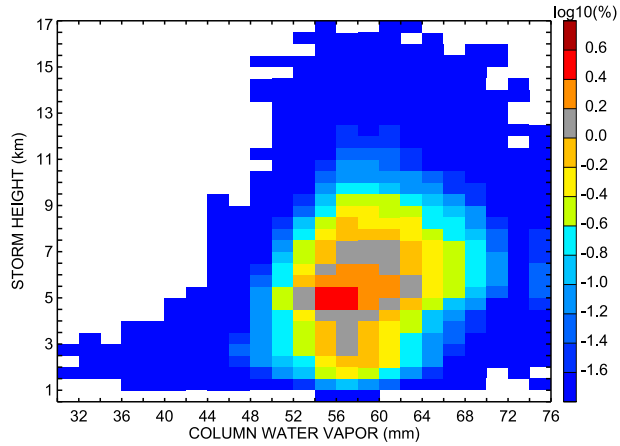

FIG. 10. TRMM PR storm height (highest radar echo top) vs TMI CWV for pixels diagnosed by the PR rain algorithm as convective for the same region (5°N–10°S, 65°–170°E) and set of MJO events (September–May of 2006–2010) analyzed by Del Genio et al. (2012a).

weaker but nonnegligible top-heavy heating and drying in the 85°–110°E region. Top-heavy heating combined with the increase of moist static energy with height above the midtroposphere minimum implies that the GCM is exporting moist static energy and stabilizing the column ahead of the precipitation peak, the opposite of that required for development of a moisture mode (Raymond et al. 2009). Cold pool I, on the other hand, produces a lower-level heating peak in the disturbed region and little net heating in the 85°–110°E region. Convective moistening of the lower free troposphere occurs as convection vertically transports moisture evaporated from the ocean surface.

Figure 12 shows the evolution of CWV and 500-hPa vertical velocity anomalies for AR5 and cold pool I. AR5 CWV and vertical velocity anomalies are small and only loosely correlated. Subsidence in part of the 85°–110°E region on day 1 gives way on day 2 to a weak rising motion anomaly, probably a response to the premature onset of deep convection there. Cold pool I on the other hand has closely coupled CWV and vertical velocity anomalies. Gradual moistening of the 85°–110°E region over the first week occurs as anomalous latent heat fluxes (not shown) increase, accompanied by gradual weakening of subsidence and eventually a transition to anomalous rising. This suggests that vertical advection plays an indirect role in the eventual onset of this MJO in the model; shallow convective moistening offsets subsidence drying until the latter weakens. This is consistent with the DYNAMO budget analysis by Ruppert and Johnson (2015), who show that subsidence weakens late in the suppressed phase, while relative humidity at 500 hPa is still very dry (~30%) and surface rain is negligible. Midlevel convective heating does increase slightly in the suppressed region in cold pool I from day 1 to day 7, so some of the large-scale vertical velocity evolution may be a response to increased convective heating rather than a cause of it. However, other sources of subsidence weakening are possible. For example, MJO onset may be triggered by weakening subsidence from circumnavigating dry Kelvin waves formed from previous MJOs that eventually impinge on the onset region from the west (Haertel et al. 2015; Powell and Houze 2015).

Hovmöller diagrams of 850- and 200-hPa zonal wind anomalies (Fig. 13) are consistent with the behavior of 500-hPa vertical velocity. East of the initial disturbed region, anomalous easterlies/westerlies are present at 850/200 hPa, respectively. Together with the precipitation and vertical velocity anomalies, this resembles the Gill-like (Gill 1980) pattern of Kelvin wave response east of a heating anomaly that is seen during MJO events

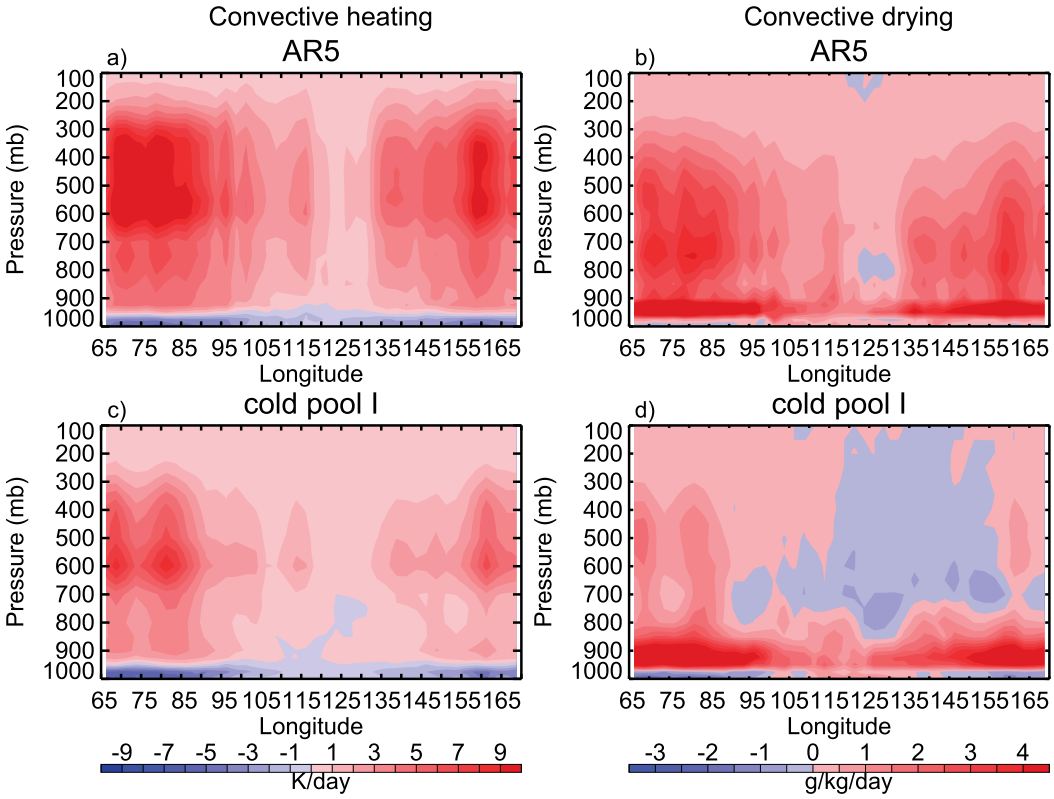

FIG. 11. Longitudinal cross sections of (a),(c) convective heating and (b),(d) convective drying for day 1 of the AR5 (a),(b) and cold pool I (c),(d) simulations.

(e.g., Virts and Wallace 2010; Powell and Houze 2013; Sobel et al. 2014). In AR5, the initial zonal wind anomaly weakens after the first 3 days, whereas in cold pool I it strengthens and remains strong for 10–12 days as the pattern propagates east, weakening only when it reaches the Maritime Continent late in week 2.

In cold pool I, the zonal source/sink of moisture in the suppressed region is dominated by advection of mean CWV (not shown, but similar to that observed in Fig. 9) by anomalous low-level easterlies (Fig. 13c). Both strengthen westward across the suppressed region, implying that zonal advection is a sink of moisture there. Meridional wind anomalies at 850 hPa (not shown) are of the wrong sign to moisten the 85°–95°E region and are weak from 95° to 110°E.

c. *Moist static energy sources and feedback strength*

If the MJO is a moisture mode, two possible column-integrated sources of moist static energy can destabilize it if the gross moist stability is positive: anomalous radiative heating (e.g., Bony and Emanuel 2005) and surface turbulent fluxes (e.g., Sobel et al. 2010). These must be in phase with the precipitation anomaly to be an effective source. Observations suggest that radiative heating is in phase with precipitation while surface fluxes lag the precipitation peak and are thus less effective (Lin and Mapes 2004; Tromeur and Rossow 2010; Sobel et al. 2014).

To evaluate the realism of the GCM MJO amplitude, we examine frequency distributions of positive precipitation anomalies in TRMM datasets and the GCM hindcasts (Fig. 14). The TRMM products differ in details but agree that for the region and time period we analyze and for our anomaly definition (see section 2), the most frequent rain anomalies are ~3 mm day^{-1}. Our two best MJO models (stronger entrainment, cold pool I) simulate the observed peak, while AR5 peaks at smaller rain rates (~1 mm day^{-1}) and cold pool II at larger (but still too small) rain rates (~2 mm day^{-1}), consistent with our previous impressions about the fidelity of each simulation.

Figures 15 and 16 show anomalies in outgoing longwave radiation (the largest contributor to column radiative heating anomalies) and surface latent heat flux (the dominant contributor to the surface turbulent flux over ocean) versus precipitation anomalies in observations (ISCCP for OLR, OAFlux for latent heat flux, and TRMM 3B42 for precipitation) and for the GCMs,

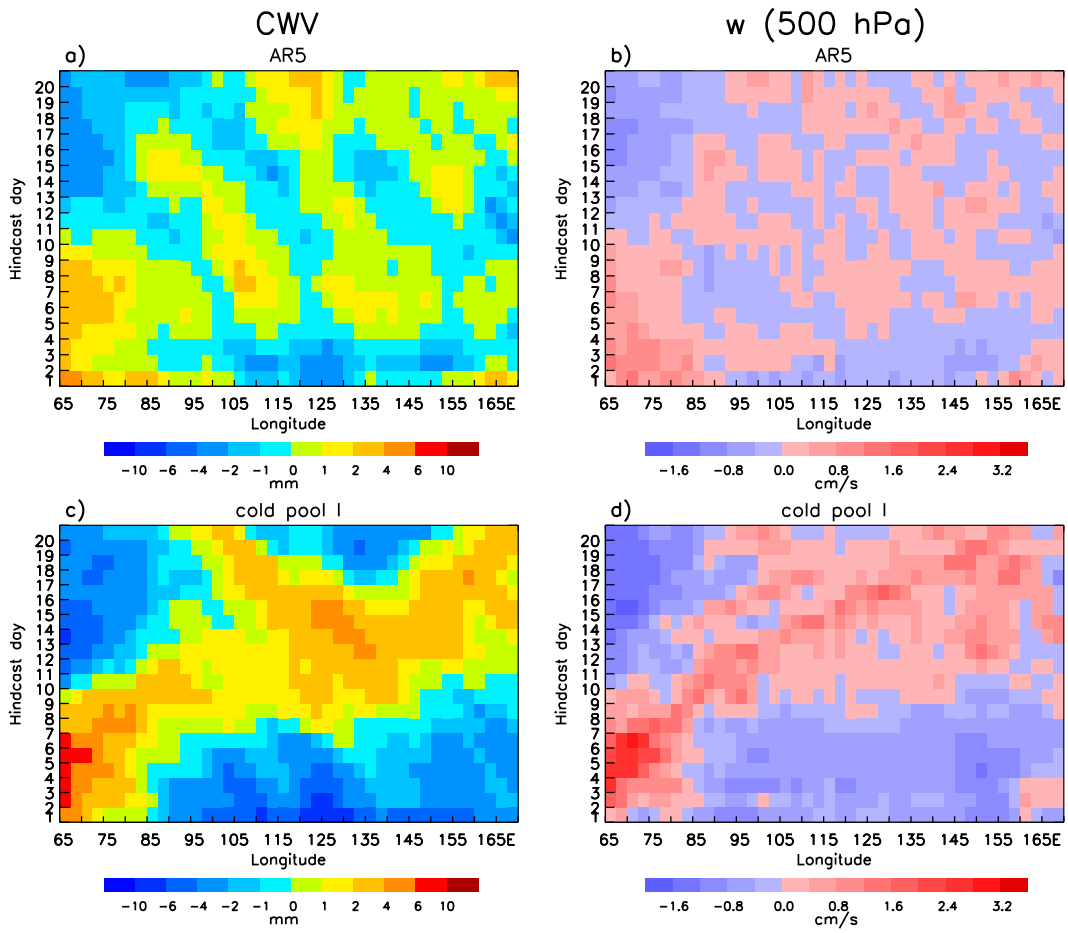

FIG. 12. Composite hindcast Hovmöller diagrams of (a),(c) CWV and (b),(d) 500-hPa vertical velocity anomalies (positive upward) for the AR5 (a),(b) and cold pool I (c),(d) simulations.

respectively. Table 2 shows the corresponding slope of the linear fits to the flux versus rain anomalies and associated correlations. These provide one measure of the feedback strength due to each source of moist static energy. All models have a strong correlation between OLR and precipitation anomalies. AR5 predictably has the smallest OLR anomalies and weakest OLR–rain correlation, while the other runs have correlations similar to those observed. The slopes of the fits (0.10–0.12) are similar to those derived from the observations and by Lin and Mapes (2004) from field experiment data. The largest OLR anomalies occur in cold pool II.

The correlation between latent heat flux and precipitation anomalies is smaller than that for OLR in observations and all the models, consistent with previous studies. For model versions that have an MJO, latent heat flux anomalies correlate best with the westerly wind bursts (e.g., positive 850-hPa zonal wind anomalies after day 7 in Fig. 13c) that lag the peak in convection. The models exhibit a somewhat stronger relation of latent heat flux to rain (0.10–0.22) than is seen in the observations (0.07), with some variation from one model version to another. Cold pool II exhibits the largest latent heat flux anomalies and the highest correlation between these and precipitation of all model versions, while the simulation that most suppresses deep convection (cold pool I) has the weakest correlation between latent heat flux and precipitation anomalies.

5. Discussion

We have shown that a conventional cumulus parameterization can simulate both the observed behavior of convection at the process level (specifically, the dependence of convection depth on humidity) and the onset, strength, and propagation of an observed MJO event that results at larger scales. Consistent with previous climatological studies of GCMs, success is contingent upon the presence of sufficient entrainment to limit the depth of convection when the troposphere is relatively dry.

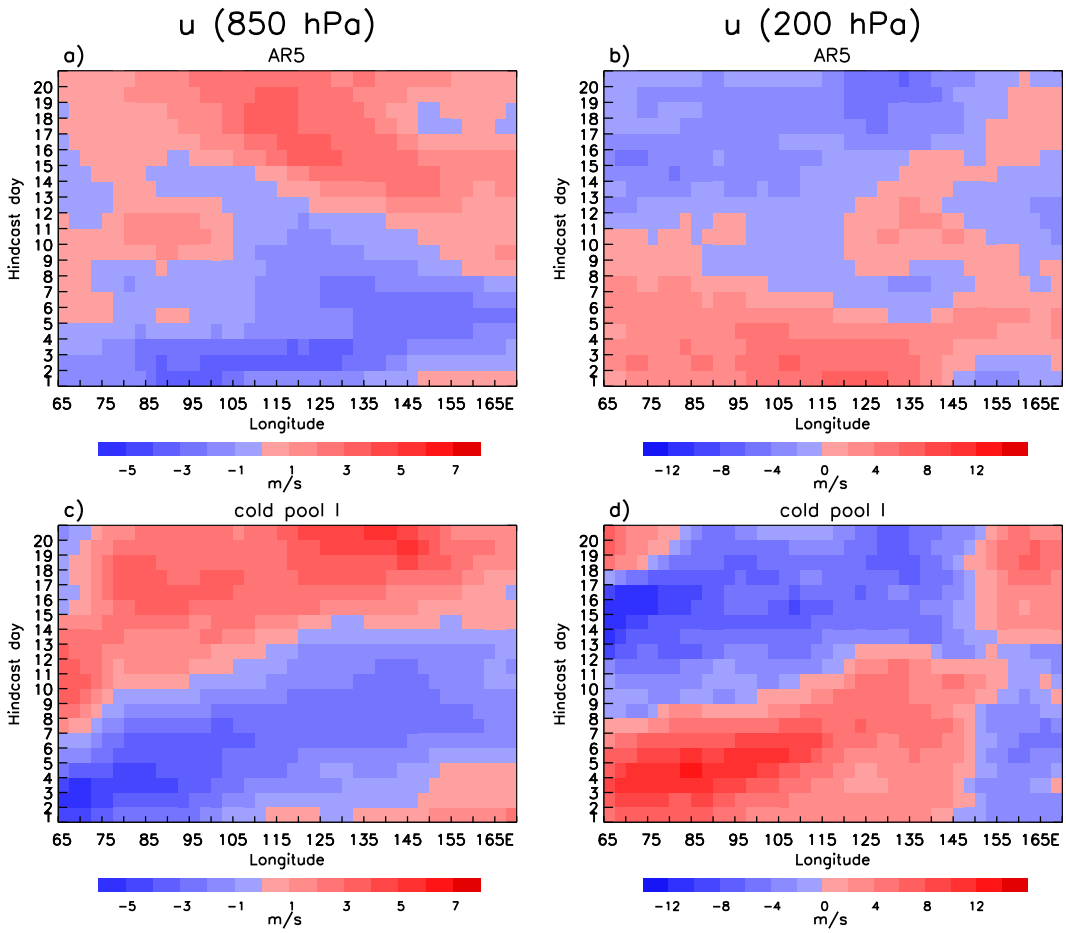

FIG. 13. As in Fig. 12, but for (a),(c) 850-hPa and (b),(d) 200-hPa zonal wind anomalies.

Given this robust conclusion across a number of GCMs, it may appear surprising that few of today's operational GCMs can simulate the MJO (Jiang et al. 2015). One impediment has been the degradation of the mean state (a wetter tropics) that occurs with stronger entrainment (Kim et al. 2011b). We have reduced model mean-state biases caused by stronger entrainment and rain evaporation by changing cloud formation thresholds to restore radiation balance, which reduces some of the excess precipitation that occurs, and by strengthening our convective downdraft, which otherwise would weaken in the more humid climate. The resulting mean state is in most respects at least comparable to the baseline model (e.g., Stanfield et al. 2014).

That having been said, fidelity of the mean state is a poor metric for many aspects of climate change (Flato et al. 2014). The MJO offers the promise of being a more useful metric, since it directly tests the interaction between convection depth, humidity, and clouds and may speak to whether the large differences among climate models in upper tropospheric clouds and humidity in convecting regions (e.g., Su et al. 2013) are significant for predictions of climate change. By itself, though, producing an MJO is not sufficient for climate models. Our SCM shows that simply strengthening entrainment does not solve all cumulus parameterization problems. In particular, model versions with a better MJO do not simulate the deepest clouds detected by the KAZR at Gan (Fig. 4 vs Fig. 5). Hannah and Maloney (2014) show that it is possible to get an MJO in DYNAMO hindcasts with compensating errors in entrainment and cloud-radiative heating. Thus, for the MJO to be a useful test of moist convection and cloud parameterizations, diagnostics of both (Figs. 4 and 5 and Figs. 15 and 16, respectively) are needed.

Our experimental cold pool parameterization aims to more physically differentiate the situations in which deep convection is and is not suppressed. Cold pool I, which produces the best MJO, underestimates the depth of convection in humid conditions (Fig. 5c), suggesting that even weaker entrainment rates in specific environments are required. Cold pools are only the first step

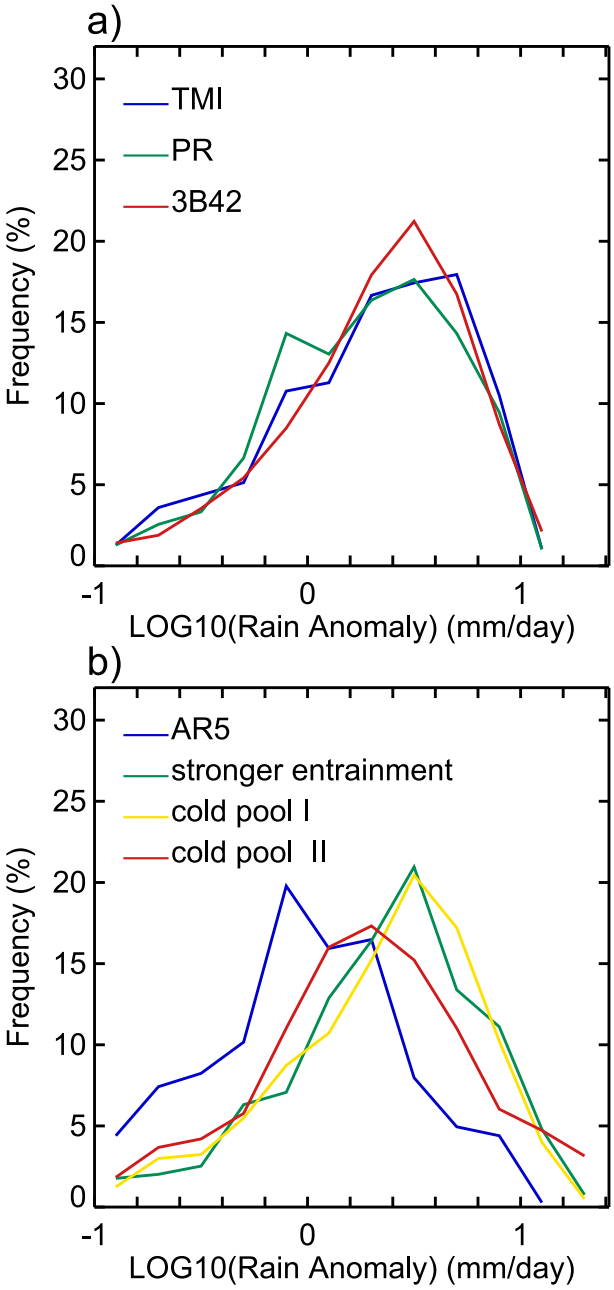

FIG. 14. Frequency of occurrence of positive rain anomalies during the hindcast period and analysis region for (a) the three TRMM rain products and (b) the four GCM versions.

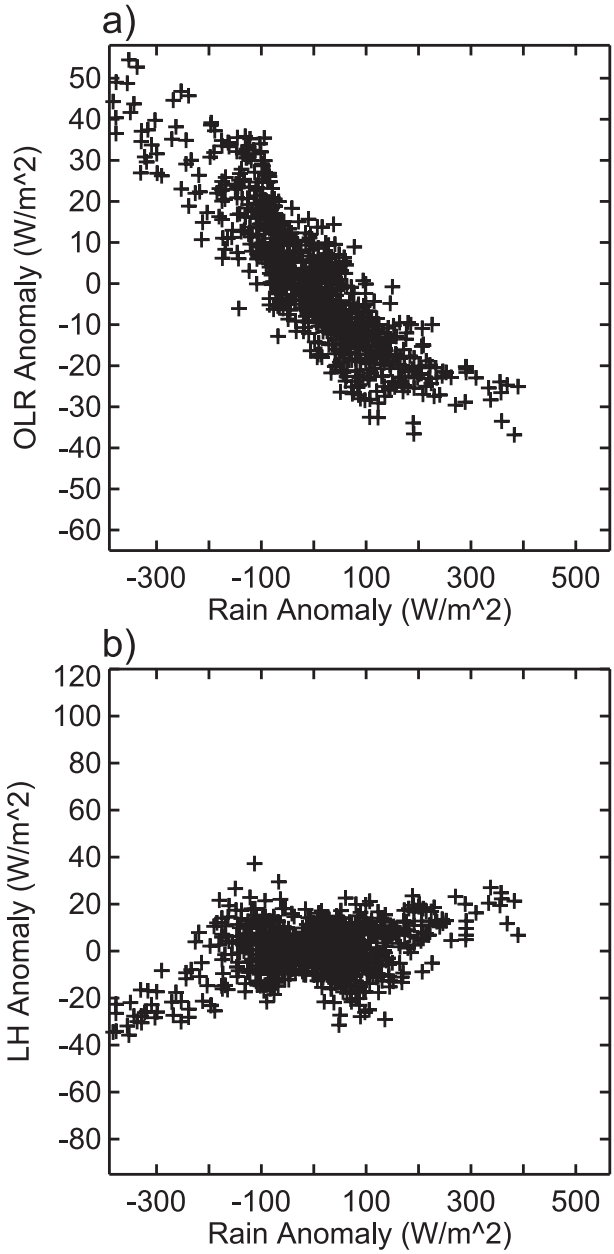

FIG. 15. (a) ISCCP OLR anomalies vs TRMM 3B42 precipitation anomalies for the hindcast period. (b) As in (a), but OAFlux latent heat flux anomalies vs TRMM 3B42 precipitation anomalies.

toward the larger goals of determining when convection should organize on the mesoscale (Del Genio et al. 2012b) and representing the clouds and precipitation that result. Organized convection is probably responsible for much of the upper-level cloudiness that produces the radiative heating anomalies that have been proposed as a driver for the MJO. Yet only one GCM parameterizes the upper-troposphere mesoscale updrafts that produce and sustain much of this cloudiness (Donner et al. 2011), and even that model does not distinguish situations in which convection does and does not organize. Is the cloud-radiative heating feedback in our "good MJO" models (Fig. 16) and others then a metric of physical realism or an example of producing correct relationships with physical processes different from those that operate in the real world?

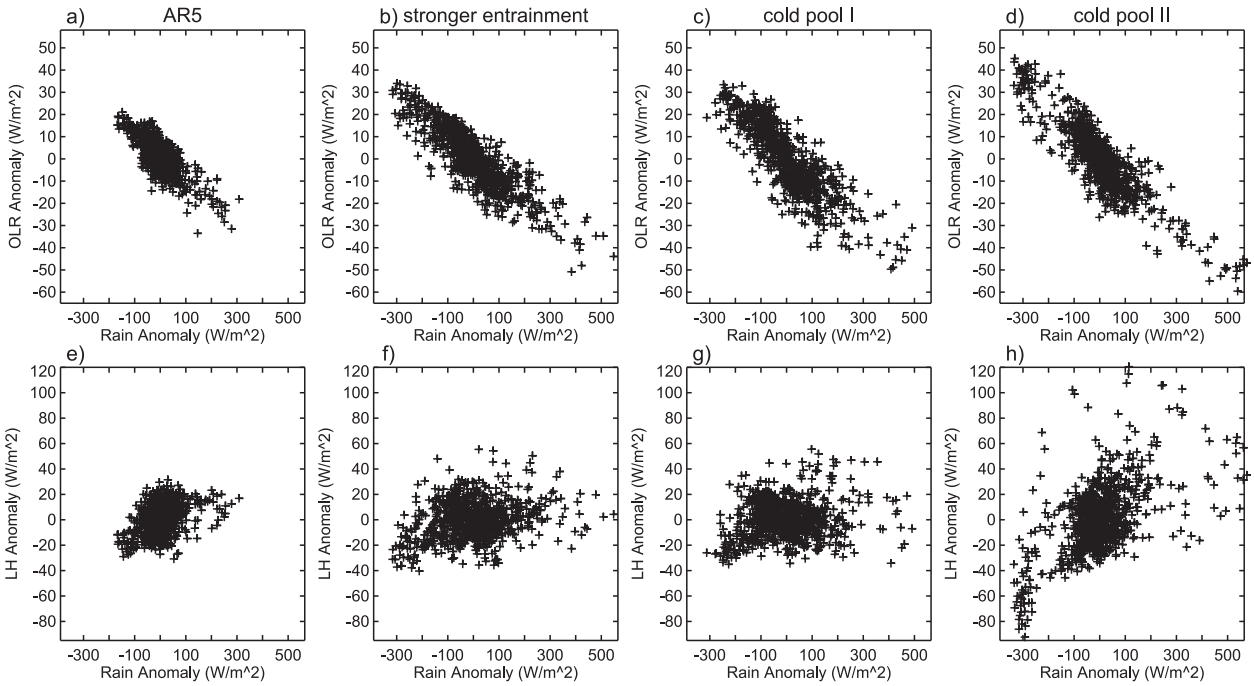

FIG. 16. Scatterplots of (a)–(d) OLR anomalies and (e)–(h) latent heat flux anomalies vs precipitation anomalies for each of the four hindcasts.

The situation may be more promising for understanding the physics of the MJO itself. Our results demonstrate clearly that dry anomalies east of the convection center are directly related to subsequent MJO onset and strength over the next 2–3 weeks (Fig. 8f). This is consistent with the conclusions of the observational analysis of Kim et al. (2014) and evidence in favor of viewing the MJO as a moisture mode. Our most successful models moisten the lower free troposphere by shallow convection east of the primary disturbed region in the week before MJO onset, by 0.5–1.0 $g\,kg^{-1}\,day^{-1}$ (Fig. 11d). This is weaker than is indicated by the moisture budget for the first DYNAMO MJO event but comparable to the second one (Ruppert and Johnson 2015). Ruppert and Johnson (2015) emphasize the importance of the diurnal cycle of SST to this moistening. Our simulations were done with prescribed diurnally invariant SST, so it is possible we underestimate the role of shallow cumulus moistening.

The more important issue may be not what shallow convection does but what it does not do. Shallow cumulus clouds heat the lower troposphere, reducing gross moist stability and perhaps changing its sign in some models (Raymond et al. 2009; Hannah and Maloney 2011; Benedict et al. 2014; Klingaman et al. 2015b). They redistribute moisture vertically but are not themselves a source of moist static energy for the preonset region. The importance of shallow convection is rather that it is not deep—that is, from the moisture mode standpoint shallow convection is a neutral response that allows sources such as surface evaporation and/or large-scale transports to slowly import moist static energy into the preonset atmosphere, eventually triggering propagation. Premature deep convection, however, quickly exports the moist static energy. In our simulations cumulus moistening and subsidence weakening appear to control the evolution of CWV in the preonset region (Figs. 12c,d). However, the relative contributions of vertical versus horizontal and zonal versus meridional advection vary from one region to another and from one MJO event to another (Ruppert and Johnson 2015; Sobel et al. 2014). Despite these differences, consistency with the basic moisture mode concept is the common feature.

Regardless of whether our anomalous high clouds are produced by the correct convective dynamics, the idea that cloud-radiative heating is a primary moist static energy source for the MJO is supported by our results. Latent heat flux anomalies lag convection in our simulations and are mostly weakly correlated with precipitation anomalies (Fig. 16; Table 2). The interesting exception is cold pool II, which has a nonnegligible correlation. Although this model version degrades the MJO relative to cold pool I, it does so only because it produces too much deep convection. In general, we expect cold pools to enhance surface turbulent heat fluxes (Tompkins 2001; Del Genio et al. 2012b). Since

TABLE 2. Relationships of anomalies in OLR and latent heat flux (LH) to precipitation anomalies in observations (ISCCP, OAFlux) and the four GCM hindcast experiments.

	$d\mathrm{OLR}'/dP'$	Correlation ($\mathrm{OLR}' - P'$)	$d\mathrm{LH}'/dP'$	Correlation ($\mathrm{LH}' - P'$)
Observations	−0.13	−0.87	0.07	0.35
AR5	−0.11	−0.77	0.20	0.36
Stronger entrainment	−0.10	−0.87	0.10	0.22
Cold pool I	−0.12	−0.86	0.16	0.14
Cold pool II	−0.12	−0.87	0.22	0.57

cold pools occur in concert with convection, it may be reasonable to expect a mesoscale latent heat flux anomaly, unrelated to the larger-scale easterlies and westerlies that accompany the MJO, to coexist with the convection in the lead-up to the MJO peak and contribute to the moist static energy source that drives it. Analysis of cold pool–related surface flux anomalies observed during DYNAMO as a function of MJO phase should help determine the role they play, if any, in MJO onset.

Acknowledgments. This research was supported by the NASA Modeling and Analysis Program through an RTOP for GISS GCM development and Grant NNX09AK34G; by a NASA Precipitation Measurement Missions Program RTOP; by an Interagency Agreement with the U.S. Department of Energy (DOE) Atmospheric System Research Program; and by a grant from the DOE FASTER Program. We thank three anonymous reviewers for constructive comments that improved the manuscript.

APPENDIX

Cold Pool Parameterization

Our objective is not to represent the complex physics of an ensemble of cold pools, which, given the sparse information at the GCM gridbox scale, is impractical and most likely unverifiable. We seek only to portray in an idealized manner the basics of how cold pools influence convection, by 1) segregating lower from higher moist static energy air in the boundary layer so convection continues to develop, 2) providing a physically based source of additional lifting and weaker entrainment to trigger subsequent convection and allow it to penetrate deeper, and 3) allowing convection to retain memory of previous conditions and depart from quasi-equilibrium. Our approach thus borrows elements from both the simple implicit approaches of Piriou et al. (2007) and Mapes and Neale (2011) and the more complex explicit cold pool parameterizations of Qian et al. (1998), Grandpeix and Lafore (2010), and Park (2014).

A cold pool is initiated if a convective downdraft reaches the boundary layer with a mass of at least 5% of the boundary layer mass and virtual potential temperature at least 0.5°C colder than that of the ambient boundary layer. If so, two new prognostic variables, the cold pool potential temperature θ_c and specific humidity q_c, are initialized as those of the downdraft air, whose mass becomes the initial cold pool mass m_c.

From these, several two-dimensional diagnostic quantities are calculated. The undisturbed boundary layer thermodynamic properties θ_u and q_u are defined as the mass-weighted difference between the gridbox mean θ and q and those of the cold pool:

$$\theta_u = (\theta - \alpha_c\theta_c)/(1 - \alpha_c), \quad \text{and} \tag{A1}$$

$$q_u = (q - \alpha_c q_c)/(1 - \alpha_c), \tag{A2}$$

where $\alpha_c = m_c/m$ is the ratio of the mass of cold pool air to the total mass of the boundary layer m. These properties define the parcel that is lifted to test for cold pool triggering of plume 1 rather than the gridbox mean properties. For simplicity, θ_c, θ_u and q_c, q_u are assumed to be homogeneous within the cold pool and undisturbed parts of the boundary layer. We define the cold pool and undisturbed virtual potential temperatures as

$$\theta_{vc} = \theta_c(1 + 0.608q_c), \quad \text{and} \tag{A3}$$

$$\theta_{vu} = \theta_u(1 + 0.608q_u). \tag{A4}$$

The cold pool spreads at a velocity v_c based on the density current speed

$$v_c = k[gh_c(\theta_{vu} - \theta_{vc})/\theta_{vu}]^{1/2}, \tag{A5}$$

where g is the acceleration of gravity, h_c is a third new prognostic variable representing the cold pool depth (p_c in pressure units), and k is an internal Froude number usually taken to be <1. For a GCM cumulus parameterization, v_c is not the spread rate of an individual downdraft density current but rather that of an ensemble of cold pools that interact to a greater or lesser extent depending on the subgrid organization of individual convective cells. When multiple cells are in close

proximity (e.g., owing to wind shear or at an airmass boundary in weak shear), their cold pools collide, deepen more, and spread less rapidly than when they are separated (Rotunno et al. 1988; Houston and Wilhelmson 2011; Feng et al. 2015). For the experiments presented here we use a fairly low value of k (0.5 for cold pool I, 0.25 for cold pool II), which assumes some interaction between individual cold pools and promotes cold pool deepening, more so for cold pool II.

We assume for simplicity a circular collective cold pool area of radius r_c that spreads radially at the velocity v_c and introduce a fourth prognostic variable, the cold pool area A_c, which increases over a time step dt at a rate given by

$$dA_c = 2\pi r_c v_c dt. \tag{A6}$$

Cold pool pressure depth p_c then evolves at each subsequent time step according to two competing effects: deepening due to subsequent downdraft mass injections dm_d

$$dp_c = g dm_d / A_c \tag{A7a}$$

and shallowing due to the cold pool horizontal spread

$$p_c^{\text{new}} = p_c^{\text{old}} A_c^{\text{old}} / A_c^{\text{new}}. \tag{A7b}$$

We ignore the additional deepening from entrainment into the top of the cold pool, but this can easily be added to Eq. (A7a). The parameter p_c is then used to calculate parcel lifting in the test for triggering of plume 1 after downdrafts terminate. We also increase the initial vertical velocity of an updraft that forms in this way, but in practice this has little effect. In experiment cold pool I, we initialize p_c to be 100 hPa when a cold pool forms, while in cold pool II, we use the boundary layer depth. Once convective downdrafts terminate, the cold pool continues to exist and p_c evolves according to Eqs. (A7a) and (A7b) with $dm_d = 0$, producing additional memory.

Cold pool thermodynamic properties evolve in two ways: properties of subsequent downdrafts (θ_d, q_d) mix with existing cold pool properties, and surface turbulent fluxes gradually restore the cold pool to ambient conditions. Rather than calculating actual cold pool surface flux perturbations, which are the integrated result of surface–air interactions at a variety of wind speeds and air conditions over many cold pools, we simply relax the cold pool properties to those of the undisturbed boundary layer with a specified relaxation time scale τ, as done by Mapes and Neale (2011) for their idealized organization parameter. Thus, θ_c and q_c change at rates given by

$$d\theta_c = (\theta_c m_c + \theta_d dm_d)/(m_c + dm_d) - \theta_c - (\theta_c - \theta_u)dt/\tau,$$

and

$$dq_c = (q_c m_c + q_d dm_d)/(m_c + dm_d) - q_c - (q_c - q_u)dt/\tau. \tag{A8, A9}$$

We take $\tau = 3$ h over ocean and 12 h over land, based on inferences from cloud-resolving model studies (Del Genio et al. 2012b). When $\theta_{vc} - \theta_{vu} > -0.5°C$, the cold pool is terminated and boundary layer properties are homogenized. The resulting climatological properties of cold pools in the cold pool II model version are shown in Del Genio et al. (2013).

REFERENCES

Andersen, J. A., and Z. Kuang, 2012: Moist static energy budget of MJO-like disturbances in the atmosphere of a zonally symmetric aquaplanet. *J. Climate,* **25,** 2782–2804, doi:10.1175/JCLI-D-11-00168.1.

Barnes, H. C., and R. A. Houze Jr., 2013: The precipitating cloud population of the Madden-Julian Oscillation over the Indian and west Pacific Oceans. *J. Geophys. Res. Atmos.,* **118,** 6996–7023, doi:10.1002/jgrd.50375.

Benedict, J. J., and D. A. Randall, 2007: Observed characteristics of the MJO relative to maximum rainfall. *J. Atmos. Sci.,* **64,** 2332–2354, doi:10.1175/JAS3968.1.

——, E. D. Maloney, A. H. Sobel, and D. M. W. Frierson, 2014: Gross moist stability and MJO simulation skill in three full-physics GCMs. *J. Atmos. Sci.,* **71,** 3327–3349, doi:10.1175/JAS-D-13-0240.1.

Bladé, I., and D. L. Hartmann, 1993: Tropical intraseasonal oscillation in a simple nonlinear model. *J. Atmos. Sci.,* **50,** 2922–2939, doi:10.1175/1520-0469(1993)050<2922:TIOIAS>2.0.CO;2.

Böing, S. J., H. J. J. Jonker, A. P. Siebesma, and W. W. Grabowski, 2012: Influence of the subcloud layer on the development of a deep convective ensemble. *J. Atmos. Sci.,* **69,** 2682–2698, doi:10.1175/JAS-D-11-0317.1.

Bony, S., and K. A. Emanuel, 2005: On the role of moist processes in tropical intraseasonal variability: Cloud–radiation and moisture–convection feedbacks. *J. Atmos. Sci.,* **62,** 2770–2789, doi:10.1175/JAS3506.1.

Chen, Y., and A. D. Del Genio, 2009: Evaluation of tropical cloud regimes in observations and a general circulation model. *Climate Dyn.,* **32,** 355–369, doi:10.1007/s00382-008-0386-6.

Chikira, M., and M. Sugiyama, 2013: Eastward-propagating intraseasonal oscillation represented by Chikira–Sugiyama cumulus parameterization. Part I: Comparison with observation and reanalysis. *J. Atmos. Sci.,* **70,** 3920–3939, doi:10.1175/JAS-D-13-034.1.

Davies, L., R. S. Plant, and S. H. Derbyshire, 2009: A simple model of convection with memory. *J. Geophys. Res.,* **114,** D17202, doi:10.1029/2008JD011653.

Del Genio, A. D., 2012: Representing the sensitivity of convective cloud systems to tropospheric humidity in general circulation models. *Surv. Geophys.,* **33,** 637–656, doi:10.1007/s10712-011-9148-9.

——, and J. Wu, 2010: The role of entrainment in the diurnal cycle of continental convection. *J. Climate,* **23,** 2722–2738, doi:10.1175/2009JCLI3340.1.

——, M.-S. Yao, W. Kovari, and K. K.-W. Lo, 1996: A prognostic cloud water parameterization for global climate models. *J. Climate,* **9,** 270–304, doi:10.1175/1520-0442(1996)009<0270:APCWPF>2.0.CO;2.

——, W. Kovari, M.-S. Yao, and J. Jonas, 2005: Cumulus microphysics and climate sensitivity. *J. Climate,* **18,** 2376–2387, doi:10.1175/JCLI3413.1.

——, M.-S. Yao, and J. Jonas, 2007: Will moist convection be stronger in a warmer climate? *Geophys. Res. Lett.,* **34,** L16703, doi:10.1029/2007GL030525.

——, Y. Chen, D. Kim, and M.-S. Yao, 2012a: The MJO transition from shallow to deep convection in *CloudSat*/CALIPSO data and GISS GCM simulations. *J. Climate,* **25,** 3755–3770, doi:10.1175/JCLI-D-11-00384.1.

——, J. Wu, and Y. Chen, 2012b: Characteristics of mesoscale organization in WRF simulations of convection during TWP-ICE. *J. Climate,* **25,** 5666–5688, doi:10.1175/JCLI-D-11-00422.1.

——, M.-S. Yao, J. Wu, and A. Wolf, 2013: Cold pools—A first step in representing convective organization in GCMs. [Available online at http://asr.science.energy.gov/meetings/stm/posters/view?id=784.]

DePasquale, A., C. Schumacher, and A. Rapp, 2014: Radar observations of MJO and Kelvin wave interactions during DYNAMO/CINDY2011/AMIE. *J. Geophys. Res. Atmos.,* **119,** 6347–6367, doi:10.1002/2013JD021031.

Derbyshire, S. H., I. Beau, P. Bechtold, J.-P. Grandpeix, J.-M. Piriou, J.-L. Redelsperger, and P. M. M. Soares, 2004: Sensitivity of moist convection to environmental humidity. *Quart. J. Roy. Meteor. Soc.,* **130,** 3055–3079, doi:10.1256/qj.03.130.

Donner, L. J., and Coauthors, 2011: The dynamical core, physical parameterizations, and basic simulation characteristics of the atmospheric component AM3 of the GFDL global coupled model CM3. *J. Climate,* **24,** 3484–3519, doi:10.1175/2011JCLI3955.1.

Feng, Z., S. Hagos, A. K. Rowe, C. D. Burleyson, M. N. Martini, and S. P. de Szoeke, 2015: Mechanisms of convective cloud organization by cold pools over tropical warm ocean during the AMIE-DYNAMO field campaign. *J. Adv. Model. Earth Syst.,* **7,** doi:10.1002/2014MS000384, in press.

Flato, G., and Coauthors, 2014: Evaluation of climate models. *Climate Change 2013: The Physical Science Basis,* T. F. Stocker et al., Eds., Cambridge University Press, 741–866.

Gill, A. E., 1980: Some simple solutions for heat-induced tropical circulation. *Quart. J. Roy. Meteor. Soc.,* **106,** 447–462, doi:10.1002/qj.49710644905.

Gottschalck, J., P. Roundy, C. Schreck, A. Vintzileos, and C. Zhang, 2013: Large-scale atmospheric and oceanic conditions during the 2011–12 DYNAMO field campaign. *Mon. Wea. Rev.,* **141,** 4173–4196, doi:10.1175/MWR-D-13-00022.1.

Grandpeix, J.-Y., and J. P. Lafore, 2010: A density current parameterization coupled with Emanuel's convection scheme. Part I: The models. *J. Atmos. Sci.,* **67,** 881–897, doi:10.1175/2009JAS3044.1.

Gregory, D., 2001: Estimation of entrainment rate in simple models of convective clouds. *Quart. J. Roy. Meteor. Soc.,* **127,** 53–72, doi:10.1002/qj.49712757104.

——, R. Kershaw, and P. M. Inness, 1997: Parametrization of momentum transport by convection. II: Tests in single-column and general circulation models. *Quart. J. Roy. Meteor. Soc.,* **123,** 1153–1183, doi:10.1002/qj.49712354103.

Haertel, P., K. Straub, and A. Budsock, 2015: Transforming circumnavigating Kelvin waves that initiate and dissipate the Madden–Julian oscillation. *Quart. J. Roy. Meteor. Soc.,* doi:10.1002/qj.2461, in press.

Hannah, W. M., and E. D. Maloney, 2011: The role of moisture–convection feedbacks in simulating the Madden–Julian oscillation. *J. Climate,* **24,** 2754–2770, doi:10.1175/2011JCLI3803.1.

——, and ——, 2014: The moist static energy budget in NCAR CAM5 hindcasts during DYNAMO. *J. Adv. Model. Earth Syst.,* **6,** 420–440, doi:10.1002/2013MS000272.

Hohenegger, C., and C. S. Bretherton, 2011: Simulating deep convection with a shallow convection scheme. *Atmos. Chem. Phys.,* **11,** 10 389–10 406, doi:10.5194/acp-11-10389-2011.

Houston, A. L., and R. B. Wilhelmson, 2011: The dependence of storm longevity on the pattern of deep convection initiation in a low-shear environment. *Mon. Wea. Rev.,* **139,** 3125–3138, doi:10.1175/MWR-D-10-05036.1.

Hu, Q., and D. A. Randall, 1994: Low-frequency oscillations in radiative–convective systems. *J. Atmos. Sci.,* **51,** 1089–1099, doi:10.1175/1520-0469(1994)051<1089:LFOIRC>2.0.CO;2.

Huffman, G. J., and Coauthors, 2007: The TRMM Multisatellite Precipitation Analysis: Quasi-global, multiyear, combined-sensor precipitation estimates at fine scales. *J. Hydrometeor.,* **8,** 38–55, doi:10.1175/JHM560.1.

Hung, M.-P., J.-L. Lin, W. Wang, D. Kim, T. Shinoda, and S. J. Weaver, 2013: MJO and convectively coupled equatorial waves simulated by CMIP5 climate models. *J. Climate,* **26,** 6185–6214, doi:10.1175/JCLI-D-12-00541.1.

Iguchi, T., T. Kozu, R. Meneghini, J. Awaka, and K. Okamoto, 2000: Rain-profiling algorithm for the TRMM precipitation radar. *J. Appl. Meteor.,* **39,** 2038–2052, doi:10.1175/1520-0450(2001)040<2038:RPAFTT>2.0.CO;2.

Jensen, M. P., and A. D. Del Genio, 2003: Radiative and microphysical characteristics of deep convective systems in the tropical western Pacific. *J. Appl. Meteor.,* **42,** 1234–1254, doi:10.1175/1520-0450(2003)042<1234:RAMCOD>2.0.CO;2.

——, and ——, 2006: Factors limiting convective cloud-top height at the ARM Nauru Island climate research facility. *J. Climate,* **19,** 2105–2117, doi:10.1175/JCLI3722.1.

Jiang, X., and Coauthors, 2015: Vertical structure and physical processes of the Madden-Julian oscillation: Exploring key model physics in climate simulations. *J. Geophys. Res. Atmos.,* **120,** 4718–4748, doi:10.1002/2014JD022375.

Johnson, R. H., and P. E. Ciesielski, 2013: Structure and properties of Madden-Julian oscillations deduced from DYNAMO sounding arrays. *J. Atmos. Sci.,* **70,** 3157–3179, doi:10.1175/JAS-D-13-065.1.

Kelley, O. A., J. Stout, M. Summers, and E. J. Zipser, 2010: Do the tallest convective cells over the tropical ocean have slow updrafts? *Mon. Wea. Rev.,* **138,** 1651–1672, doi:10.1175/2009MWR3030.1.

Kemball-Cook, S. R., and B. C. Weare, 2001: The onset of convection in the Madden–Julian oscillation. *J. Climate,* **14,** 780–793, doi:10.1175/1520-0442(2001)014<0780:TOOCIT>2.0.CO;2.

Khairoutdinov, M. F., and D. A. Randall, 2006: High-resolution simulation of shallow-to-deep convection transition over land. *J. Atmos. Sci.,* **63,** 3421–3436, doi:10.1175/JAS3810.1.

Kim, D., and Coauthors, 2009: Application of MJO simulation diagnostics to climate models. *J. Climate,* **22,** 6413–6436, doi:10.1175/2009JCLI3063.1.

——, A. H. Sobel, and I.-S. Kang, 2011a: A mechanism denial study on the Madden-Julian Oscillation. *J. Adv. Model. Earth Syst.,* **3,** M12007, doi:10.1029/2011MS000081.

——, ——, E. D. Maloney, D. M. W. Frierson, and I.-S. Kang, 2011b: A systematic relationship between intraseasonal variability and mean state bias. *J. Climate,* **24,** 5506–5520, doi:10.1175/2011JCLI4177.1.

——, ——, A. Del Genio, Y. Chen, S. J. Camargo, M.-S. Yao, M. Kelley, and L. Nazarenko, 2012: The tropical subseasonal variability simulated in the NASA GISS general circulation model. *J. Climate,* **25,** 4641–4659, doi:10.1175/JCLI-D-11-00447.1.

——, A. D. Del Genio, and M.-S. Yao, 2013: Moist convection scheme in Model E2. 9 pp. [Available online at http://www.giss.nasa.gov/tools/modelE/docs/kim_moistconvection.pdf.]

——, J.-S. Kug, and A. H. Sobel, 2014: Propagating versus nonpropagating Madden–Julian oscillation events. *J. Climate,* **27,** 111–125, doi:10.1175/JCLI-D-13-00084.1.

——, M.-S. Ahn, I.-S. Kang, and A. D. Del Genio, 2015: Role of longwave cloud–radiation feedback in the simulation of the Madden–Julian oscillation. *J. Climate,* doi:10.1175/JCLI-D-14-00767.1, in press.

Kiranmayi, L., and E. D. Maloney, 2011: Intraseasonal moist static energy budget in reanalysis data. *J. Geophys. Res.,* **116,** D21117, doi:10.1029/2011JD016031.

Klingaman, N. P., and Coauthors, 2015a: Vertical structure and physical processes of the Madden-Julian oscillation: Linking hindcast fidelity to simulated diabatic heating and moistening. *J. Geophys. Res. Atmos.,* **120,** 4690–4717, doi:10.1002/2014JD022374.

——, X. Jiang, P. K. Xavier, J. Petch, D. Waliser, and S. J. Woolnough, 2015b: Vertical structure and physical processes of the Madden-Julian oscillation: Synthesis and summary. *J. Geophys. Res. Atmos.,* **120,** 4671–4689, doi:10.1002/2015JD023196.

Lau, K.-M., and H.-T. Wu, 2010: Characteristics of precipitation, cloud, and latent heating associated with the Madden–Julian oscillation. *J. Climate,* **23,** 504–518, doi:10.1175/2009JCLI2920.1.

Lin, J.-L., and B. E. Mapes, 2004: Radiation budget of the tropical intraseasonal oscillation. *J. Atmos. Sci.,* **61,** 2050–2062, doi:10.1175/1520-0469(2004)061<2050:RBOTTI>2.0.CO;2.

——, and Coauthors, 2006: Tropical intraseasonal variability in 14 IPCC AR4 climate models. Part I: Convective signals. *J. Climate,* **19,** 2665–2690, doi:10.1175/JCLI3735.1.

Lin, X., and R. H. Johnson, 1996: Kinematic and thermodynamic characteristics of the flow over the western Pacific warm pool during TOGA COARE. *J. Atmos. Sci.,* **53,** 695–715, doi:10.1175/1520-0469(1996)053<0695:KATCOT>2.0.CO;2.

Ma, D., and Z. Kuang, 2011: Modulation of radiative heating by the Madden-Julian oscillation and convectively coupled Kelvin waves as observed by CloudSat. *Geophys. Res. Lett.,* **38,** L21813, doi:10.1029/2011GL049734.

Madden, R. A., and P. Julian, 1971: Detection of a 40–50 day oscillation in the zonal wind in the tropical Pacific. *J. Atmos. Sci.,* **28,** 702–708, doi:10.1175/1520-0469(1971)028<0702:DOADOI>2.0.CO;2.

Majda, A. J., and S. N. Stechmann, 2009: The skeleton of tropical intraseasonal oscillations. *Proc. Natl. Acad. Sci. USA,* **106,** 8417–8422, doi:10.1073/pnas.0903367106.

Maloney, E. D., 2009: The moist static energy budget of a composite tropical intraseasonal oscillation in a climate model. *J. Climate,* **22,** 711–729, doi:10.1175/2008JCLI2542.1.

Mapes, B., 2000: Convective inhibition, subgrid-scale triggering energy, and stratiform instability in a toy tropical wave model. *J. Atmos. Sci.,* **57,** 1515–1535, doi:10.1175/1520-0469(2000)057<1515:CISSTE>2.0.CO;2.

——, and R. Neale, 2011: Parameterizing convective organization to escape the entrainment dilemma. *J. Adv. Model. Earth Syst.,* **3,** M06004, doi:10.1029/2011MS000042.

Matsuno, T., 1966: Quasi-geostrophic motions in the equatorial area. *J. Meteor. Soc. Japan,* **44,** 25–43.

Mauritsen, T., and Coauthors, 2012: Tuning the climate of a global model. *J. Adv. Model. Earth Syst.,* **4,** M00A01, doi:10.1029/2012MS000154.

McFarlane, S. A., C. N. Long, and D. M. Flynn, 2005: Impact of island-induced clouds on surface measurements: Analysis of the ARM Nauru Island Effect Study data. *J. Appl. Meteor.,* **44,** 1045–1065, doi:10.1175/JAM2241.1.

Morita, J., Y. N. Takayabu, S. Shige, and Y. Kodama, 2006: Analysis of rainfall characteristics of the Madden–Julian oscillation using TRMM satellite data. *Dyn. Atmos. Oceans,* **42,** 107–126, doi:10.1016/j.dynatmoce.2006.02.002.

Neelin, J. D., and J.-Y. Yu, 1994: Modes of tropical variability under convective adjustment and the Madden–Julian oscillation. Part I: Analytical theory. *J. Atmos. Sci.,* **51,** 1876–1894, doi:10.1175/1520-0469(1994)051<1876:MOTVUC>2.0.CO;2.

Park, S., 2014: A unified convection scheme (UNICON). Part I: Formulation. *J. Atmos. Sci.,* **71,** 3902–3930, doi:10.1175/JAS-D-13-0233.1.

Petch, J., D. Waliser, X. Jiang, P. Xavier, and S. Woolnough, 2011: A global model intercomparison of the physical processes associated with the Madden–Julian oscillation. *GEWEX News,* No. 21, International GEWEX Project Office, Silver Spring, MD, 3–5.

Piriou, J. M., J. L. Redelsperger, J. F. Geleyn, J. P. Lafore, and F. Guichard, 2007: An approach for convective parameterization with memory: Separating microphysics and transport in grid-scale equations. *J. Atmos. Sci.,* **64,** 4127–4139, doi:10.1175/2007JAS2144.1.

Powell, S. W., and R. A. Houze Jr., 2013: The cloud population and onset of the Madden-Julian oscillation over the Indian Ocean during DYNAMO-AMIE. *J. Geophys. Res. Atmos.,* **118,** 11 979–11 995, doi:10.1002/2013JD020421.

——, and ——, 2015: Effect of dry large-scale vertical motions on initial MJO convective onset. *J. Geophys. Res. Atmos.,* **120,** 4783–4805, doi:10.1002/2014JD022961.

Qian, L., G. S. Young, and W. M. Frank, 1998: A convective wake parameterization scheme for use in general circulation models. *Mon. Wea. Rev.,* **126,** 456–469, doi:10.1175/1520-0493(1998)126<0456:ACWPSF>2.0.CO;2.

Raymond, D. J., 2001: A new model of the Madden–Julian oscillation. *J. Atmos. Sci.,* **58,** 2807–2819, doi:10.1175/1520-0469(2001)058<2807:ANMOTM>2.0.CO;2.

——, and Ž. Fuchs, 2009: Moisture modes and the Madden–Julian oscillation. *J. Climate,* **22,** 3031–3046, doi:10.1175/2008JCLI2739.1.

——, S. Sessions, A. H. Sobel, and Ž. Fuchs, 2009: The mechanics of gross moist stability. *J. Adv. Model. Earth Syst.,* **1,** 9, doi:10.3894/JAMES.2009.1.9.

Riley, E. M., B. E. Mapes, and S. N. Tulich, 2011: Clouds associated with the Madden–Julian oscillation: A new perspective from *CloudSat*. *J. Atmos. Sci.,* **68,** 3032–3051, doi:10.1175/JAS-D-11-030.1.

Rotunno, R., J. B. Klemp, and M. L. Weisman, 1988: A theory for strong, long-lived squall lines. *J. Atmos. Sci.,* **45,** 463–485, doi:10.1175/1520-0469(1988)045<0463:ATFSLL>2.0.CO;2.

Ruppert, J. H., Jr., and R. H. Johnson, 2015: Diurnally modulated cumulus moistening in the preonset stage of the Madden–Julian oscillation during DYNAMO. *J. Atmos. Sci.,* **72,** 1622–1647, doi:10.1175/JAS-D-14-0218.1.

Schlemmer, L., and C. Hohenegger, 2014: The formation of wider and deeper clouds as a result of cold-pool dynamics. *J. Atmos. Sci.,* **71,** 2842–2858, doi:10.1175/JAS-D-13-0170.1.

Schmidt, G. A., and Coauthors, 2014: Configuration and assessment of the GISS ModelE2 contributions to the CMIP5 archive. *J. Adv. Model. Earth Syst.,* **6,** 141–184, doi:10.1002/2013MS000265.

Sherwood, S. C., D. Hernández-Deckers, M. Colin, and F. Robinson, 2013: Slippery thermals and the cumulus entrainment paradox. *J. Atmos. Sci.,* **70,** 2426–2442, doi:10.1175/JAS-D-12-0220.1.

Sobel, A., and E. D. Maloney, 2013: Moisture modes and the eastward propagation of the MJO. *J. Atmos. Sci.,* **70,** 187–192, doi:10.1175/JAS-D-12-0189.1.

——, ——, G. Bellon, and D. Frierson, 2010: Surface fluxes and tropical intraseasonal variability: A reassessment. *J. Adv. Model. Earth Syst.,* **2,** doi:10.3894/JAMES.2010.2.2.

——, S. Wang, and D. Kim, 2014: Moist static energy budget of the MJO during DYNAMO. *J. Atmos. Sci.,* **71,** 4276–4291, doi:10.1175/JAS-D-14-0052.1.

Song, H., W. Lin, Y. Lin, A. Wolf, R. Neggers, L. J. Donner, A. D. Del Genio, and Y. Liu, 2013: Evaluation of precipitation simulated by seven SCMs against the ARM observations at the SGP site. *J. Climate,* **26,** 5467–5492, doi:10.1175/JCLI-D-12-00263.1.

Stanfield, R. E., X. Dong, B. Xi, A. Kennedy, A. D. Del Genio, P. Minnis, and J. Jiang, 2014: Assessment of NASA GISS CMIP5 and post-CMIP5 simulated clouds and TOA radiation budgets using satellite observations. Part I: Cloud fraction and properties. *J. Climate,* **27,** 4189–4208, doi:10.1175/JCLI-D-13-00558.1.

Stephens, G. L., P. J. Webster, R. H. Johnson, R. Engelen, and T. L'Ecuyer, 2004: Observational evidence for the mutual regulation of the tropical hydrological cycle and tropical sea surface temperatures. *J. Climate,* **17,** 2213–2224, doi:10.1175/1520-0442(2004)017<2213:OEFTMR>2.0.CO;2.

Su, H., and Coauthors, 2013: Diagnosis of regime-dependent cloud simulation errors in CMIP5 models using "A-Train" satellite observations and reanalysis data. *J. Geophys. Res. Atmos.,* **118,** 2762–2780, doi:10.1029/2012JD018575.

Tokioka, T., K. Yamazaki, A. Kitoh, and T. Ose, 1988: The equatorial 30-60 day oscillation and the Arakawa-Schubert penetrative cumulus parameterization. *J. Meteor. Soc. Japan,* **66,** 883–901.

Tompkins, A. M., 2001: Organization of tropical convection in low vertical wind shears: The role of cold pools. *J. Atmos. Sci.,* **58,** 1650–1672, doi:10.1175/1520-0469(2001)058<1650:OOTCIL>2.0.CO;2.

Tromeur, E., and W. B. Rossow, 2010: Interaction of tropical deep convection with the large-scale circulation in the MJO. *J. Climate,* **23,** 1837–1853, doi:10.1175/2009JCLI3240.1.

Virts, K. S., and J. M. Wallace, 2010: Annual, interannual, and intraseasonal variability of tropical tropopause transition layer cirrus. *J. Atmos. Sci.,* **67,** 3097–3112, doi:10.1175/2010JAS3413.1.

Wentz, F. J., 1997: A well-calibrated ocean algorithm for special sensor microwave/imager. *J. Geophys. Res.,* **102,** 8703–8718, doi:10.1029/96JC01751.

Wheeler, M., and G. N. Kiladis, 1999: Convectively coupled equatorial waves: Analysis of clouds and temperature in the wavenumber–frequency domain. *J. Atmos. Sci.,* **56,** 374–399, doi:10.1175/1520-0469(1999)056<0374:CCEWAO>2.0.CO;2.

——, and H. H. Hendon, 2004: An all-season real-time multivariate MJO index: Development of an index for monitoring and prediction. *Mon. Wea. Rev.,* **132,** 1917–1932, doi:10.1175/1520-0493(2004)132<1917:AARMMI>2.0.CO;2.

Xie, S., R. T. Cederwall, and M. Zhang, 2004: Developing long-term single-column model/cloud system–resolving model forcing data using numerical weather prediction products constrained by surface and top of the atmosphere observations. *J. Geophys. Res.,* **109,** D01104, doi:10.1029/2003JD004045.

Xu, W., and S. A. Rutledge, 2014: Convective characteristics of the Madden–Julian oscillation over the central Indian Ocean observed by shipborne radar during DYNAMO. *J. Atmos. Sci.,* **71,** 2859–2877, doi:10.1175/JAS-D-13-0372.1.

Yao, M.-S., and Y. Cheng, 2012: Cloud simulations in response to turbulence parameterizations in the GISS Model E GCM. *J. Climate,* **25,** 4963–4974, doi:10.1175/JCLI-D-11-00399.1.

Yoneyama, K., C. Zhang, and C. N. Long, 2013: Tracking pulses of the Madden–Julian oscillation. *Bull. Amer. Meteor. Soc.,* **94,** 1871–1891, doi:10.1175/BAMS-D-12-00157.1.

Yu, L., X. Jin, and R. A. Weller, 2008: Multidecade global flux datasets from the Objectively Analyzed air-sea Fluxes (OAFlux) Project: Latent and sensible heat fluxes, ocean evaporation, and related surface meteorological variables. Woods Hole Oceanographic Institution OAFlux Project Tech. Rep. OA-2008-01, 64 pp. [Available online at http://oaflux.whoi.edu/pdfs/OAFlux_TechReport_3rd_release.pdf.]

Zhang, C., 2013: Madden–Julian oscillation: Bridging weather and climate. *Bull. Amer. Meteor. Soc.,* **94,** 1849–1870, doi:10.1175/BAMS-D-12-00026.1.

——, J. Gottschalck, E. D. Maloney, M. W. Moncrieff, F. Vitart, D. E. Waliser, B. Wang, and M. C. Wheeler, 2013: Cracking the MJO nut. *Geophys. Res. Lett.,* **40,** 1223–1230, doi:10.1002/grl.50244.

Zhang, M. H., J. L. Lin, R. T. Cederwall, J. J. Yio, and S. C. Xie, 2001: Objective analysis of ARM IOP data: Method and sensitivity. *Mon. Wea. Rev.,* **129,** 295–311, doi:10.1175/1520-0493(2001)129<0295:OAOAID>2.0.CO;2.

Zhang, Y.-C., W. B. Rossow, A. A. Lacis, V. Oinas, and M. I. Mishchenko, 2004: Calculation of radiative fluxes from the surface to top of atmosphere based on ISCCP and other global data sets: Refinements of the radiative transfer model and the input data. *J. Geophys. Res.,* **109,** D19105, doi:10.1029/2003JD004457.

Zuluaga, M. D., and R. A. Houze Jr., 2013: Evolution of the population of precipitating convective systems over the equatorial Indian Ocean in active phases of the Madden–Julian oscillation. *J. Atmos. Sci.,* **70,** 2713–2725, doi:10.1175/JAS-D-12-0311.1.